CHAMMI-75: PRE-TRAINING MULTI-CHANNEL MODELS WITH HETEROGENEOUS MICROSCOPY IMAGES

Anonymous authors
Paper under double-blind review

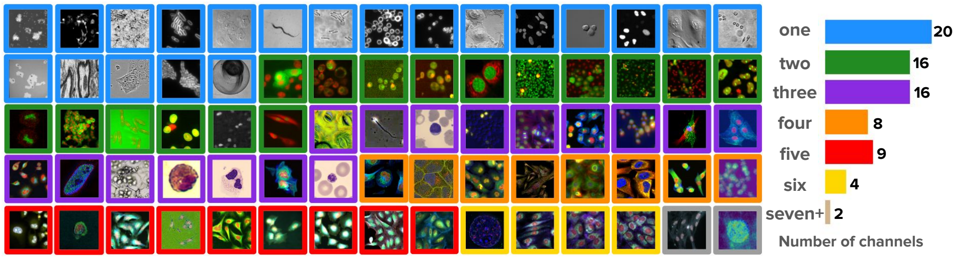

Figure 1: Example images in CHAMMI-75, a heterogenous dataset of multi-channel microscopy images. Channel colors are assigned to an RGB pseudo-color for visualization.

ABSTRACT

Quantifying cell morphology using images and machine learning has proven to be a powerful tool to study the response of cells to treatments. However, the models used to quantify cellular morphology are typically trained with a single microscopy imaging type and under controlled experimental conditions. This results in specialized models that cannot be reused across biological studies because the technical specifications do not match (e.g., different number of channels), or because the target experimental conditions are out of distribution. Here, we present CHAMMI-75, a dataset of heterogeneous, multi-channel microscopy images with 2.8M multi-channel images from 75 diverse biological studies. We curated this resource from publicly available sources to investigate cellular morphology models that are channel-adaptive and can process any microscopy image type. Our experiments show that training with CHAMMI-75 can improve performance in multi-channel bioimaging tasks, opening the way to create the next generation of cellular morphology models for biological studies.

1 INTRODUCTION

Microscopy is a versatile scientific tool in experimental biology and allows researchers to acquire images of cells under controlled experimental conditions. Unlike natural images, which are consistently acquired and stored in a three-channel, RGB format, microscopy images can have a varied number of channels; anywhere from one to dozens, each encoding a different type of signal. Deep learning is widely adopted to analyze microscopy images (Moen et al., 2019; Volpe et al., 2023; Pratapa et al., 2021; Xing et al., 2017), but the most common strategy to create such models is to modify architectures developed for RGB images by changing and fixing the number of channels according to the problem (Doron et al., 2023; Gupta et al., 2024). This limits the ability to reuse models from experiment to experiment, or to pre-train large-scale models that accumulate universal knowledge of cellular biology.

Multi-channel imaging models have emerged to address the limitations of existing vision architectures, enabling the processing of varied number of channels at test time (Kraus et al., 2024; Bourriez et al., 2024; Pham & Plummer, 2024; Pham et al., 2025). A common trend in such architectures is the separation of channels as individual modalities, resulting in flexible,

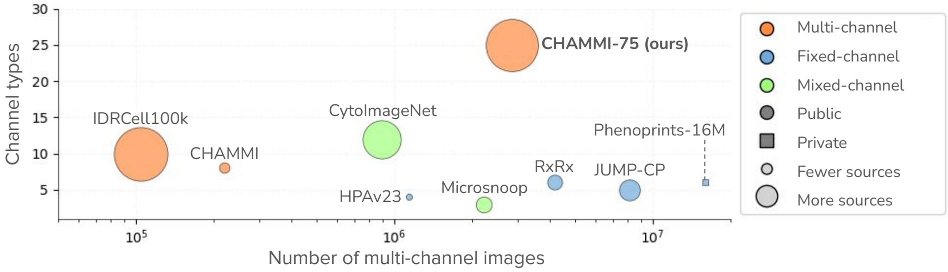

Figure 2: Comparison of existing microscopy datasets used for representation learning of cell morphology. CHAMMI-75 is the largest dataset of multi-channel microscopy images. Others datasets: IDRCell100k (Bourriez et al., 2024), CHAMMI (Chen et al., 2023), CytoImageNet (Hua et al., 2021), HPAv23 (Gupta et al., 2024), Microsnoop (Xun et al., 2024), RxRx Recursion (2025), JUMP-CP (Chandrasekaran et al., 2023a), and Phenoprints-16M (Kenyon-Dean et al., 2024).

variable-length inputs with diverse channel types. While these initiatives represent an important step towards creating foundation models for cellular imaging, most of them are still small-scale, proof-of-concept experiments. The main reason is the lack of standardized and well-curated datasets to properly test these ideas at large scale. Multi-channel microscopy images are publicly available, but it is not straightforward to put them together in a single, useful resource for machine learning research because of their technical differences, varied formats, and inconsistent metadata.

We present a new multi-channel microscopy image dataset that we call CHAMMI-75 (Figure 1). Our dataset is larger than prior work (Figure 2) and combines diverse heterogeneous sources of biological images into a single resource to investigate cellular morphology. CHAMMI-75 breaks the assumptions of most prior work focused on deep learning for bioimage analysis since it contains more technical and biological variation than typically used to train cellular imaging models (Figure 3). For example, CHAMMI-75 includes images of 16 organisms and 223 cell lines collected with different microscopes, at different resolutions, and with different numbers of channels. Our goal was to obtain a representative visual sample of the cellular biology universe that can be observed with microscopy. With the accelerated progress of machine learning, this diversity comes as a valuable source of information to train the next generation of multi-channel imaging models. Ultimately, we believe that foundation models for microscopy imaging should be able to understand cell morphology at all scales, in all cell types, and independently of the imaging technology used for observation.

This work addresses the data gap hindering the development of generalizable models for cellular imaging. Progress in machine learning is often catalyzed not only by algorithmic novelty but by the rigorous, large-scale data curation efforts that enable it. ImageNet (Deng et al., 2009) and LAION (Schuhmann et al., 2022) are prominent examples that fundamentally shifted the focus of representation learning research and supported breakthroughs that would have been impossible without such data. In computational biology, challenging and realistic data is similarly necessary to advance the field. While significant progress has been achieved with fixed-channel image models, many open problems still exist to achieve a general understanding of cellular states regardless of the imaging technology. CHAMMI-75 is the first resource to integrate heterogeneous multi-channel imaging data at this scale in a way that directly facilitates the investigation of these challenges.

The purpose of CHAMMI-75 is to facilitate the creation of models for cell phenotyping, which is the task of identifying and quantifying morphological differences between cellular states (e.g., healthy vs. perturbed cells). This goal is distinct from, but complementary to, other critical bioimage analysis tasks such as cell segmentation, where foundation models like Segment Anything for Microscopy (Archit et al., 2025) have demonstrated success in generalized mask generation across modalities. CHAMMI-75 provides the data necessary to train and evaluate models that can detect subtle biological classification signals, which cannot be achieved through segmentation alone.

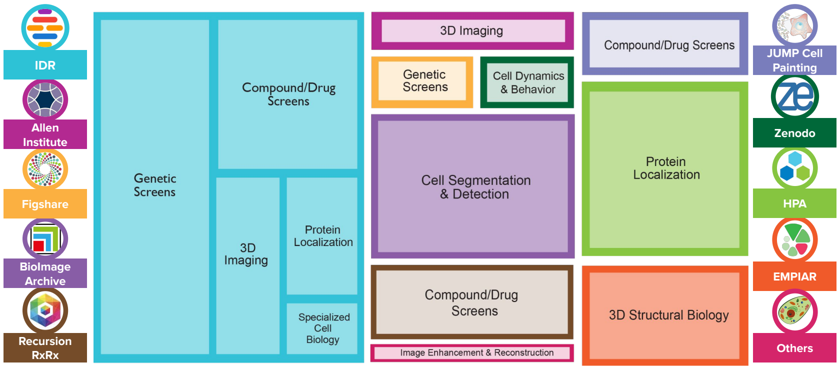

Figure 3: Diversity of sources and biological studies in `CHAMMI-75`. The treemap illustrates the distribution of images according to the hosting platforms they were obtained from (colors) and the type of biological study (inner rectangles). We sampled from 18 different sources to ensure broad coverage of biological study types.

The contributions of our work are: (1) we introduce a large, heterogeneous dataset of multi-channel microscopy images, with 25 channel types and high technical and biological variation. (2) We introduce two new datasets and benchmarks to evaluate multi-channel model performance, which represent real-world contemporary biological studies with novel channel combinations (e.g., 14-channel images). (3) We conducted a systematic experimental evaluation to investigate the usefulness of our dataset as a pre-training resource, using self-supervised learning. The experimental results show that `CHAMMI-75` yields strong models that perform well in a diverse set of challenging biological tasks. (4) We will make all the data, code, and models publicly available to allow for reproducibility of our results, and to facilitate future development in the field.

2 Related Work

Figure 2 provides a high-level overview comparison of our dataset and prior work. The biological imaging community has a long tradition of publicly sharing the datasets obtained in their studies. Prominent initiatives to store and share imaging datasets include the Image Data Repository (IDR) (Williams et al., 2017), the Bioimage Archive (Hartley et al., 2022), and the Cell Painting Gallery (Weisbart et al., 2024). Other major projects create large datasets of cells exposed to many treatments to serve as a map to investigate various biological questions. These include the RxRx datasets (Sypetkowski et al., 2023), along with the JUMP-CP dataset (Chandrasekaran et al., 2023b), which cover a large number of genetic and chemical perturbations. Similarly, the Human Protein Atlas (Thul et al., 2017), the OpenCell project (Cho et al., 2022), and Allen Institute for Cell Science (Viana et al., 2023) have created image datasets to map the localization of proteins in human cells. While all these resources have multi-channel images and are publicly available, they are typically used and analyzed separately. Closest to ours is IDRCell100k (Bourriez et al., 2024), a dataset created for multi-channel model development containing 100K images from 79 different sources. Inspired by their work, we extend the effort and scale to an order of magnitude more images and with additional data curation.

Prior work has explored channel-adaptive imaging (e.g., (Bao et al., 2023; Bourriez et al., 2024; Kraus et al., 2024; Pham & Plummer, 2024; Pham et al., 2025)), and where the number and configuration of the input channels is not fixed, they either train on private data (Kraus et al., 2024; Kenyon-Dean et al., 2024), or on small, publicly available datasets for proof-of-concept experiments (Chen et al., 2023). Other work either focuses on weakly- or self-supervised methods over fixed channels (Caicedo et al., 2018; Moshkov et al., 2024; Doron et al., 2023; Kim et al., 2025), or developing channel-agnostic methods (Carpenter et al., 2006; Caicedo et al., 2017; Pawlowski et al., 2016; Ando et al., 2017; Xun et al., 2024; Morelli et al., 2025; Lian et al., 2025; De Lorenci et al., 2025). These studies provided

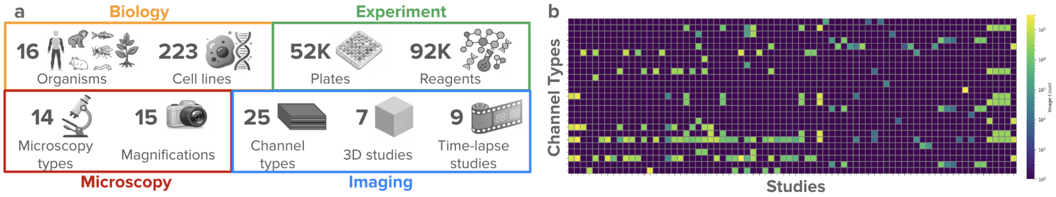

Figure 4: Content and distribution of images in `CHAMMI-75` according to the integrated metadata. a) Selected metadata fields and summary statistics of their diversity. b) Sparse, long-tail distribution of channel configurations across studies. None of the studies has all channel types, and none of the channels is used in all studies.

insight into how image-based profiling can reveal the response of cells to biological reagents (Caicedo et al., 2016), and it can be scaled to high-throughput experiments using robotic automation (Boutros et al., 2015). As our dataset contains varying numbers of channels, our experiments use representatives of both channel-agnostic and channel-adaptive modeling.

3 The `CHAMMI-75` Dataset

`CHAMMI-75` is a collection of 2,849,483 fields-of-view (FoV) sampled from 75 publicly available microscopy imaging studies; 74 sources used for pre-training data and one source held out for evaluation only. Each FoV in the pre-training set is a multi-channel microscopy image with up to seven channels, and may have a single or multiple cells (Figure 1). Our dataset is the largest multi-channel image dataset for model pre-training in microscopy. Compared to existing microscopy imaging datasets, `CHAMMI-75` draws from many more sources and contains many more channel types (Figure 2), opening new opportunities to investigate multi-channel models at large scale.

The process of building `CHAMMI-75` followed three major phases. We started with a *data acquisition* phase for selecting hosting platforms, identifying source datasets, downloading raw data, and standardizing image formats. Next, we conducted a *metadata integration* phase where all the experimental details of the downloaded images were collected, organized, and integrated across all sources. The final phase was *data curation*, which focused on strategically sampling the most representative and informative images for learning. This phase transformed the downloaded image set collected in the first phase into `CHAMMI-75`.

Data acquisition. The `CHAMMI-75` dataset was collected from 18 different hosting platforms that store biological images from published scientific studies (Figure 3). The top 5 sources of imaging data according to the number of studies obtained are: The Image Data Resource (IDR) (Williams et al., 2017), Zenodo (CERN & OpenAIRE, 2013), Mendeley Data (Elsevier, 2025), Figshare (Singh, 2011), and RxRx (Recursion, 2025). Other prominent sources of high-quality imaging data include: The Cell Painting Gallery (Weisbart et al., 2024), the BioImage Archive (Hartley et al., 2022), the Human Protein Atlas (HPA) (Thul et al., 2017), the Broad Bioimage Benchmark Collection (Ljosa et al., 2012), and the Allen Institute for Cell Science (Viana et al., 2023). These repositories provide access to image datasets created by biological labs around the world with open data licenses; 97% of datasets in our collection have a Creative Commons license (65% CC BY 4.0, 12% CC0 1.0). More details in Table A6.

From these hosting platforms, we selected 75 source datasets with highly heterogeneous biological and technical settings. Biological diversity was defined in terms of organisms and types of perturbations, while technical diversity was defined in terms of microscopy techniques and imaging settings (Figure 4). More details of the data acquisition pipeline in Appendix A.1.

Metadata integration. We collected metadata information to prepare consistent information for guiding the sampling of high-quality, diverse images for the pre-training set. Not all images are equally informative or useful, and we targeted biological and technical variables reported in the original studies for filtering purposes. As a result, the metadata

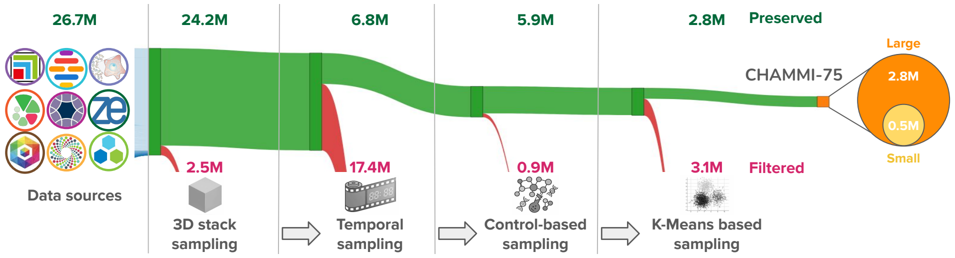

Figure 5: Dataset curation pipeline. Left: the dataset downloaded from the hosting platforms. Middle: the metadata is used to filter redundancy by randomly sampling a few: 2D slices from 3D images, frames from live microscopy videos, and wells from control conditions. Right: content-based clustering selects diverse, high-quality images as a final step to create `CHAMMI-75`.

table has 22 columns organized in 6 groups depending on the type of information (Figures 4 and A9). These values were obtained from the original sources by parsing information from (1) available resource descriptor files, (2) values encoded in image filenames, and (3) details reported in the source paper. Most studies have a scientific publication that describes experimental details, and for part of the metadata preparation, we used large-language models to assist with the identification and organization of certain information. The final metadata was parsed programmatically using deterministic rules and then manually curated and validated. (Appendix A.3).

Data curation. Data curation is an important effort to successfully scale representation learning (Vo et al., 2024; Siméoni et al., 2025). Our goal was to select a diverse sample that represents the main factors of variation in the ∼26M downloaded images. To this end, we systematically sampled images following information in the metadata table. Figure 5 illustrates the main steps of the dataset curation, designed to minimize redundancy and select informative images from all sources. The main filtering steps include 3D stack sampling, temporal sampling, control-based sampling, and K-means based filtering (Appendix A.2). By carefully curating images in this way, we selected 2.8M diverse multi-channel images from multiple sources, resulting in the pre-training dataset `CHAMMI-75`.

Content annotations. We analyzed image contents to produce annotations about the locations of single cells. Specifically, we configured cell segmentation pipelines for all sources using Cellpose (Stringer et al., 2021; Pachitariu & Stringer, 2022) primarily to detect the nucleus (when available) or the cell body. We recorded the center of mass coordinates for 1.8B single cells found in the 2.8M multi-channel images. This information is useful to generate crops that contain visible cells during training, thus avoiding empty, noisy, or non-informative regions. More details are reported in the Appendix A.8.

4 Evaluation benchmarks

Here we briefly describe six datasets and associated evaluation tasks that we adopt for performance evaluation, which represent real-world, contemporary image-based biological studies. Details about the benchmarks are reported in Figure 6 and in Appendix A.9.

CHAMMI benchmark. This benchmark (Chen et al., 2023) contains about 220K multi-channel images in three subsets with different numbers and types of channels, and includes six out-of-domain generalization tasks. The tasks include: cell-cycle stage classification (3 channels, WTC-11 dataset), protein localization classification (4 channels, HPA dataset), and replicate treatment retrieval (5 channels, LINCS Cell Painting dataset). We follow the standard evaluation protocol and report the CHAMMI score.

IDR-0017. A chemical-genetic interaction study (Breinig et al., 2015) that includes 150K two-channel images of 12 cell-lines treated with 1,280 compounds. The task is to identify hits among the combinatorial experiments by ranking gene-compound combinations that are likely to have a large effect with respect to controls. Ground truth hits were obtained

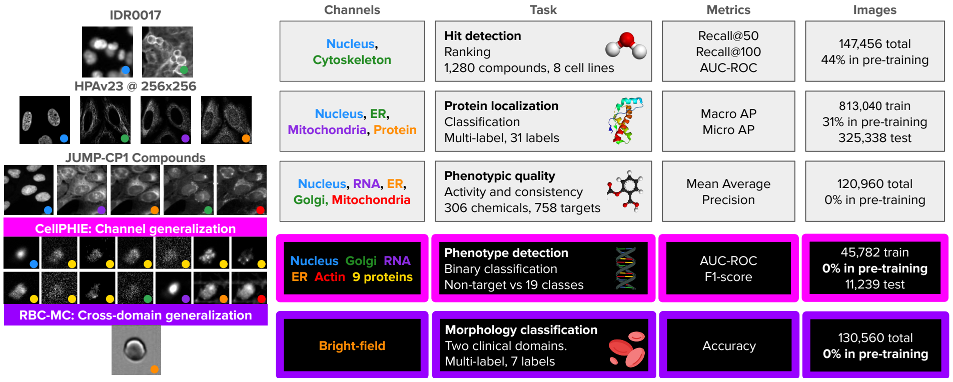
IDR0017
HPAv23 @ 256x256
JUMP-CP1 Compounds
CellPHIE: Channel generalization
RBC-MC: Cross-domain generalization

Channels	Task	Metrics	Images
Nucleus, Cytoskeleton	**Hit detection** Ranking 1,280 compounds, 8 cell lines	Recall@50 Recall@100 AUC-ROC	147,456 total 44% in pre-training
Nucleus, ER, Mitochondria, Protein	**Protein localization** Classification Multi-label, 31 labels	Macro AP Micro AP	813,040 train 31% in pre-training 325,338 test
Nucleus, RNA, ER, Golgi, Mitochondria	**Phenotypic quality** Activity and consistency 306 chemicals, 758 targets	Mean Average Precision	120,960 total 0% in pre-training
Nucleus Golgi RNA ER Actin 9 proteins	**Phenotype detection** Binary classification Non-target vs 19 classes	AUC-ROC F1-score	45,782 train **0% in pre-training** 11,239 test
Bright-field	**Morphology classification** Two clinical domains. Multi-label, 7 labels	Accuracy	130,560 total **0% in pre-training**

Figure 6: Illustration of the evaluation sets in CHAMMI-75. We adopted existing benchmarks (HPAv23 (Gupta et al., 2024) and JUMP-CP1 (Chandrasekaran et al., 2023a)), and introduce three new from real biological studies (IDR0017 (Breinig et al., 2015), CellPHIE (Kang et al., 2025), and RBC-MC (Doan et al., 2020)) for channel and cross-domain generalization.

from the original study, and performance is evaluated using recall at the top 50 and 100 items of a ranked list and AUROC.

HPAv23 at 256×256. HPA studies the localization of proteins in human cells by classifying images of cells into the correct localization category (Ouyang et al., 2019; Le et al., 2022). We adopt the latest version of the dataset, HPAv23, with 1.1 million images of single cells and annotations for protein localization classification in 19 or 31 classes. The original image size is 1024x1024, and we reduced it to 256x256 to accelerate benchmarking. We preserve the rest of the benchmark intact, and report average precision scores accordingly.

JUMP-CP1 Compounds. We adopt a subset of the JUMP-CP (Chandrasekaran et al., 2023b) dataset, which includes 24K five-channel images of U2OS cells perturbed with 306 chemicals at two time points. There are two ranking tasks in this benchmark: 1) phenotypic activity: identify compounds with a response significantly different from negative controls, and 2) phenotypic consistency: measures whether groups of biologically related compounds are clustered together. We report mean average precision for both tasks.

CellPHIE. A pooled genetic perturbation screen to investigate Huntington's Disease (Kang et al., 2025), this dataset contains 57K 14-channel images of single cells perturbed with one of 19 genes. A non-targetting control is used as a reference to determine the effect of perturbations. The task is to classify single cells in a binary classification setting: non-targetting vs perturbed gene. Images from this dataset are not included in the pretraining dataset, resulting in a novel channel combination benchmark.

Red Blood Cell Morphology Classification (RBC-MC). A set of 130,560 single-channel bright-field images (48x48 pixels) of RBCs obtained via imaging flow cytometry from two distinct clinical sites (Swiss and Canadian blood banks) (Doan et al., 2020). The task is a multi-class classification into seven clinically relevant morphological categories associated with blood quality. The benchmark employs a cross-domain validation protocol with a linear probe trained on data from one site and tested on the other (Swiss vs Canadian).

5 Experiments and Results

We identify two main multi-channel strategies that are emerging in recent work: (1) Bag of channels (BoC) models, which train backbone networks that read one channel at a time and then concatenate features for downstream tasks. Examples of this strategy include Microsnoop (Xun et al., 2024), uniDINO (Morelli et al., 2025), and DINO-BoC (De Lorenci et al., 2025). (2) Multi-channel attention (MCA) models, which unravel channel tokens into a single, long sequence to model cross-channel associations. This includes models such as Channel-ViT (Bao et al., 2023), CA-MAE (Kraus et al., 2024), and ChA-MAEViT (Pham

Table 1: Performance of models across benchmarks. Column legend: **mcT**: Multi-channel training, **mcM**: Multi-channel mechanism (✋ manual selection of channel combination, 👜 bag of channels, 🚂 variable-length sequence of channel tokens), **Dataset**: Pre-training dataset, **CM**: CHAMMI, **H**: HPAv23 256x256, **J1**: JUMP-CP1, **J2**: JUMP-CP2, **I**: IDR0017, **CP**: CellPHIE (channel generalization), **R**: RBC-MC (cross-domain generalization). All models are ViT-small and have been trained with SSL, except for the top-line results of SubCell (gray row), which is a collection of specialized, larger models (ViT-base) trained with multi-objective, weakly supervised learning. The result of best performing SubCell model for each benchmark is presented. Numbers in bold are best result among SSL methods. Bold numbers: best result across methods.

	Model Characteristics			Benchmarks ↑						
Model	**mcT**	**mcM**	**Dataset**	**CM**	**H**	**J1**	**J2**	**I**	**CP**	**R**
SubCell	×	✋	🔬 HPAv23	*53.38*	*69.33*	*77.60*	*07.44*	*24.94*	*71.23*	*59.10*
DINOv2	×	👜	📷 LVD-142M	37.93	53.76	75.84	**07.03**	25.20	72.27	59.41
OpenPhenom	✓	🚂	🔬 RxRx + JUMP	38.22	49.13	74.26	04.99	25.24	75.56	64.43
IDRCell	✓	👜	🔬 IDRCell100k	37.38	44.05	72.37	04.97	24.42	79.14	55.85
DINO-BoC	✓	👜	🔬 CHAMMI-75 L	**48.75**	**58.87**	**76.32**	06.79	**25.53**	**80.51**	**68.34**

et al., 2025), among others (Pham & Plummer, 2024; Bourriez et al., 2024). Here, we benchmark ViT models with the BoC approach, and analyze their scalability properties together with Channel-ViT as a representative architecture of MCA models.

5.1 Benchmarking experiments

We trained a ViT-small model with DINO-BoC (De Lorenci et al., 2025) on CHAMMI-75 and compare the results against existing models used to obtain representations of cellular images. Performance is measured in the six benchmarks described in Section 4.

Baselines. We consider state-of-the-art pre-trained models that have been recently released for cellular image analysis. We start with SubCell (Gupta et al., 2024), a suit of ViT-base models trained with the HPAv23 dataset using multi-objective, weakly supervised learning. SubCell has four fixed-channel models (one 2ch, two 3ch, one 4ch) trained in two modes (MAE-Cells, ViT-ProtS). The eight SubCell models exhibit excellent performance in downstream tasks; however, their usage requires manual configuration to decide a channel combination and model type. The variation of results between SubCell models is substantial (Appendix D.1.1), making its usage challenging and computationally expensive to test in practice. We also evaluate OpenPhenom (Kraus et al., 2024), a channel adaptive ViT-small model trained on five and six-channel Cell Painting images, and DINOv2 (Oquab et al., 2023), which is a fixed RGB channel model adapted for multi-channel images using BoC. Finally, we trained a model with the best configuration found in the scaling evaluation but adapted for IDRCell100K (Bourriez et al., 2024), a multi-channel microscopy image dataset close to ours in number of sources (79 vs 75) but smaller (100k multi-channel images).

Results. Table 1 shows pre-training channel-adaptive architectures with SSL yields models that are generally useful in many tasks, regardless of the number of channels. SubCell sets top-line results across several benchmarks; its strong performance may be explained by factors such as training with biological objectives, larger ViT models, channel specialization, and manual selection of best results across their different settings. Our BoC model trained with CHAMMI-75 obtained the best performance in six out of seven benchmarks, demonstrating generalization in tasks with varying channel configurations. The same model trained with IDRCell100k (a multi-channel microscopy image dataset) underperforms in most tasks, suggesting that CHAMMI-75 contains additional informative images and higher quality data for learning. OpenPhenom also underperforms in several tasks, and while it is channel adaptive, it was trained exclusively with Cell Painting data (RxRx & JUMP-CP) using MAE. Overall, our model exhibits strong performance in challenging tasks thanks to a combination of simple methods and high-quality, well-curated data.

5.2 Channel Generalization and Cross Modality Transfer

We explore channel generalization through the most challenging and realistic scenarios encountered in biological practice. First, generalization to *novel channel combinations*, which is very frequent in laboratories by combining known channels in novel ways. The CellPHIE (CP) benchmark, with its unique 14-channel configuration, serves as a real-world test for this capability. Second, generalization to *novel modalities and domains*. The RBC-MC (R) benchmark tests this by using single-channel bright-field imaging flow cytometry (modality) to classify red blood cell morphologies. Importantly, its paired cross-domain evaluation across clinical sites, challenges models to encode biologically relevant features.

The results, summarized in the last two columns of Table 1, strongly validate our approach: the model trained with `CHAMMI-75` (DINO-BoC) yields the best performance in both generalization challenges. This performance contrasts sharply with highly specialized models like SubCell, which lags behind when faced with these novel conditions. Specifically, our smaller, SSL-trained model outperforms the larger, WSL-trained SubCell by 11% in CellPHIE and 13% in RBC-MC. This result confirms that the large scale and diversity of `CHAMMI-75` are essential factors for achieving robust channel and domain generalization.

5.3 Factors impacting representation learning

To understand which factors of the heterogeneous `CHAMMI-75` dataset drive robust representation learning, we performed five targeted data ablation studies, systematically controlling and contrasting key metadata variables while measuring performance across the six out-of-distribution generalization tasks in the CHAMMI benchmark. These experiments revealed a clear hierarchy of factors that influence model performance (Figure 7). First, specialized vs. heterogeneous data: the single largest factor is the sheer diversity of the training data. Models trained with specialized data from a single task show a 40% relative performance drop compared to models trained on the full, heterogeneous `CHAMMI-75` set. This strongly suggests that generalized knowledge gained from broad exposure outweighs highly specific, small-scale training. More details in Appendix B.

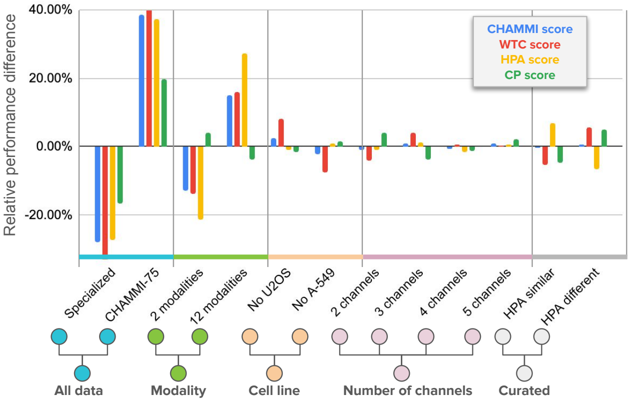

Figure 7: Data ablation study with five factors of variation. Heterogeneity and microscopy type (modality) are the main drivers of performance improvements in `CHAMMI-75`.

The second most influential factor is the diversity of imaging modality (microscopy type). When we contrasted a model trained only on the two most dominant and similar modalities (fluorescence and epi-fluorescence) against a model trained on the remaining twelve less-represented modalities, the high-diversity modality model outperformed the dominant-modality model by a 13% relative margin. This is a powerful finding that confirms our initial hypothesis: it is the exposure to a broad range of technical acquisition methods, rather than high volume within a narrow setup, that compels the model to learn truly generalizable representations. Variations in frequent biological factors, such as training without the most common cell line (U2OS or A549), or limiting training by the number of channels (e.g., training only on studies with up to two, three, or four channels), resulted in minor or negligible performance changes ($\sim 1-3\%$) across the generalization tasks. This indicates that while highly diverse cell lines and varied channel counts contribute to overall robustness, the diversity of the physical imaging process (modality) is the primary technical variable that forces the model to learn a deeper, more abstract morphology.

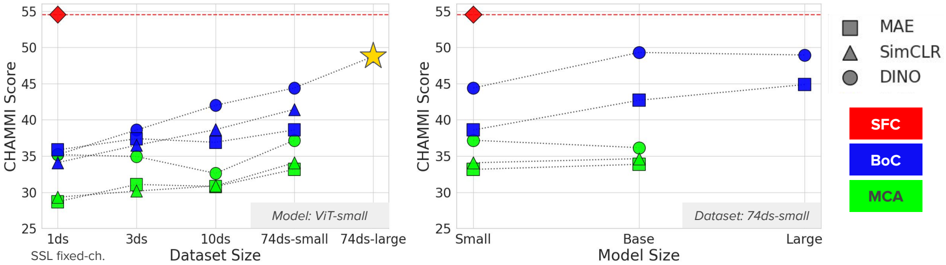

Figure 8: Scaling properties of self-supervised, multi-channel models. Dataset and model scaling results on the CHAMMI benchmark. SFC supervised fixed-channels, BoC bag of channels, MCA multi-channel attention, ⭐ model scaled with best configuration.

5.4 Scalability analysis

We evaluate `CHAMMI-75` as a pre-training resource through two main evaluations. (a) Dataset scaling: we assess performance on the CHAMMI benchmark (six out-of-distribution, phenotype matching tasks) by increasing the amount of multi-channel images used for training. Baselines include specialized models (1ds, ∼33K images, 3, 4, or 5 channels). We then combine sets: 3 CHAMMI subsets (3ds, 100K images, 8 channels), 10 datasets (10ds, 178K images, 14 channels), and a sample of `CHAMMI-75` (74ds-small, 560K images, 25 channels). The full `CHAMMI-75` set (74ds-large, 2.8M images, 25 channels) is used only for the main benchmarking. (b) Model scaling: we fix the dataset size (74ds-small) and increase model parameters. In all cases, we train ViT models, BoC (single channel) and MCA (variable channels), with a 224x224 input size using three SSL algorithms (SimCLR, MAE, DINO). Hyperparameters are kept consistent where possible. After SSL training, features are extracted from the CHAMMI test sets with frozen weights and no finetuning. Mode experimental details in the Appendix C and G.2.

Consistent with prior work, models trained with SSL benefit from more data. Comparing SSL performance against fully-supervised, specialized models (an upper bound), our results (Figure 8) confirm that as data and model size increase, SSL models approach the specialized supervised performance. This shows a single, scaled, unsupervised multi-channel model can be highly competitive. The primary performance determinant is the multi-channel strategy (BoC or MCA), followed by the SSL algorithm and model size. BoC models outperform MCA in the SSL regime, suggesting difficulty in learning cross-channel correlations unsupervised. BoC models are also easier to scale, as MCA requires 3X to 5X more GPU hours due to longer sequences (Figure G21). Among algorithms, DINO consistently performs best. Based on these findings, we trained a BoC ViT-small model using DINO on the full `CHAMMI-75` dataset (5X larger), requiring 2,352 GPU hours. This yielded a 9.8% relative improvement over the best result from the dataset scaling evaluation, with potential for further gains using larger ViT architectures, which were not explored.

5.5 Weakly supervised learning

Table 2: Performance of WSL models ChA-MAEViT (Pham et al., 2025) and MCA-SupC (Khosla et al., 2020) across benchmarks, with a DINO-based self-supervised model (MCA-SSL) included for comparison.

	Benchmarks ↑					
Model	**CM**	**H**	**J1**	**J2**	**I**	**CP**
MCA-SSL	37.18	37.46	61.72	01.85	24.40	67.93
MCA-SupC	36.15	51.81	72.72	05.20	**25.21**	75.59
ChA-MAEViT	**38.72**	**56.92**	**74.99**	**05.53**	24.99	**76.12**

The state-of-the-art in image-based profiling introduces prior knowledge of biological conditions using weakly supervised learning (WSL) with objectives such as treatment or protein classification (Gupta et al., 2024; Moshkov et al., 2024). While these pretext tasks are not focused on the primary model use, they improve performance as long as the labels are clean and consistent enough to facilitate learning. Table 2 evaluates two WSL models trained with 74ds-small using the CHAMMI-75 reagent identifier (see Appendix A.4). We find WSL method ChAMAEViT (Pham et al., 2025) obtains best performance, demonstrating the ability of CHAMMI-75 to benefit multiple learning strategies.

5.6 Additional Analysis

Our experimental analysis was designed to isolate the impact of core design choices under the self-supervised pre-training regime, which is necessary to leverage large, heterogeneous datasets without consistent supervised labels. Our results suggest the following model factors impacting performance: (1) Multi-channel strategy: the BoC approach proved to be more effective and scalable under the SSL regime, yielding up to 19% relative improvement over MCA, which also has a high computational cost. (2) SSL method: among the tested methods, DINO was the top-performing algorithm, showing a 15% relative improvement over MAE and a 7% relative improvement over SimCLR (Figure 8a). (3) Model size: we observed consistent performance gains from model scaling. Moving from ViT-Small to ViT-Large models resulted in a relative improvement of 9% to 11% (Figure 8b). (4) The use of weak supervision, even with noisy labels, improved performance by 1-19% relative to the baseline in the MCA setting. These results provide guidance for future research on multi-channel models as the field continues to bridge the gap between self-supervised and supervised performance.

Finally, we conducted an evaluation of biological feature disentanglement using the batch correction framework of Arevalo et al. (2024). The results indicate that features learned with CHAMMI-75 are more robust to technical variation (requiring less batch correction) while maximizing biological signal. Following correction with the Seurat CCA algorithm (Stuart et al., 2019), our features achieve high separation of biological (compound) clusters from technical (laboratory) batches, performing better than features extracted by CellProfiler features and those learned from the IDRCell100K dataset. This validates that CHAMMI-75 is a high-quality resource for learning disentangled features. This finding is further supported by the qualitative analysis of our feature space (Appendix F), where UMAP visualizations of single-channel features confirm that the primary clustering factor is the source study (technical domain). This domain-sensitive learning indicates that models successfully encode the immense heterogeneity of the dataset, confirming the necessity of post-processing steps like batch correction to maximize biological signal (Appendix E).

6 Conclusion and Limitations

Conclusion. We introduced CHAMMI-75, a dataset of heterogeneous multi-channel microscopy images for pre-training cellular image analysis models. The dataset combined images from 75 diverse sources, resulting in a curated, high-quality resource that has more biological and technical variation than other microscopy datasets used in prior work. Our dataset paves the way to investigate multi-channel imaging models at large scale, and can facilitate the development of foundation models that work seamlessly across biological labs and image configurations. We adopted existing benchmarks and introduced new ones, including a novel channel combination set, to continue evaluating progress in the ever-changing world of microscopy. Our experimental results show that CHAMMI-75 can be used to scale models that yield strong performance across the benchmarks. All the data, code, and models necessary to reproduce this research will be publicly available upon publication.

Limitations. The scaling evaluation was limited by the computational resources available in academic institutions. This work was focused on high-quality data curation and leaves the investigation of novel methods for multi-channel modeling for future research. The final metadata is informative but noisy despite best efforts to standardize all sources. This represents a real-world condition of imaging data, and generates challenges for supervised methods or similar types of studies. While the presented dataset is large and representative of many microscopy imaging types and biological conditions, it is also sparse and does not cover all relevant variables in balanced way.

Ethics Statement

We have no ethical concerns with our work. All the datasets sampled in our 75 studies have been cited with their licenses. The licensing information can be obtained in the Appendix A6. All these datasets can be used for furthering scientific research, and understanding foundation models in microscopy but not for commercial purposes.

Reproducibility Statement

For reproducibility purposes, we will release our best model weights, dataset and the code on a suitable platform upon acceptance of the paper. We hope that the community can use this work as a resource for further research into foundation models for cellular microscopy.

References

Andrea Acevedo, Anna Merino, Santiago Alférez, Ángel Molina, Laura Boldú, and José Rodellar. A dataset of microscopic peripheral blood cell images for development of automatic recognition systems. *Data in brief*, 30:105474, 2020.

D Michael Ando, Cory Y McLean, and Marc Berndl. Improving phenotypic measurements in high-content imaging screens. *BioRxiv*, pp. 161422, 2017.

Laura Antonelli, Federica Polverino, Alexandra Albu, Aroj Hada, Italia A Asteriti, Francesca Degrassi, Giulia Guarguaglini, Lucia Maddalena, and Mario R Guarracino. Alfi: Cell cycle phenotype annotations of label-free time-lapse imaging data from cultured human cells. *Scientific Data*, 10(1):677, 2023.

Anwai Archit, Luca Freckmann, Sushmita Nair, Nabeel Khalid, Paul Hilt, Vikas Rajashekar, Marei Freitag, Carolin Teuber, Melanie Spitzner, Constanza Tapia Contreras, et al. Segment anything for microscopy. *Nature Methods*, 22(3):579–591, 2025.

John Arevalo, Ellen Su, Jessica D Ewald, Robert Van Dijk, Anne E Carpenter, and Shantanu Singh. Evaluating batch correction methods for image-based cell profiling. *Nature Communications*, 15(1):6516, 2024.

Yujia Bao, Srinivasan Sivanandan, and Theofanis Karaletsos. Channel vision transformers: an image is worth 1 x 16 x 16 words. *arXiv preprint arXiv:2309.16108*, 2023.

Sumona Biswas and Shovan Barma. A large-scale optical microscopy image dataset of potato tuber for deep learning based plant cell assessment. *Scientific Data*, 7(1):371, 2020.

Alexandra Bodzas, Pavel Kodytek, and Jan Zidek. A high-resolution large-scale dataset of pathological and normal white blood cells. *Scientific Data*, 10(1):466, 2023.

Nicolas Bourriez, Ihab Bendidi, Ethan Cohen, Gabriel Watkinson, Maxime Sanchez, Guillaume Bollot, and Auguste Genovesio. Chada-vit: Channel adaptive attention for joint representation learning of heterogeneous microscopy images. In *Proceedings of the IEEE/CVF Conference on Computer Vision and Pattern Recognition*, pp. 11556–11565, 2024.

Michael Boutros, Florian Heigwer, and Christina Laufer. Microscopy-based high-content screening. *Cell*, 163(6):1314–1325, 2015.

Mark-Anthony Bray, Shantanu Singh, Han Han, Chadwick T Davis, Blake Borgeson, Cathy Hartland, Maria Kost-Alimova, Sigrun M Gustafsdottir, Christopher C Gibson, and Anne E Carpenter. Cell painting, a high-content image-based assay for morphological profiling using multiplexed fluorescent dyes. *Nat. Protoc.*, 11(9):1757–1774, September 2016.

Marco Breinig, Felix A Klein, Wolfgang Huber, and Michael Boutros. A chemical–genetic interaction map of small molecules using high-throughput imaging in cancer cells. *Molecular systems biology*, 11(12):846, 2015.

Michal Breker, Melissa Gymrek, and Maya Schuldiner. A novel single-cell screening platform reveals proteome plasticity during yeast stress responses. *Journal of Cell Biology*, 200(6): 839–850, 2013.

Juan C Caicedo, Shantanu Singh, and Anne E Carpenter. Applications in image-based profiling of perturbations. *Current opinion in biotechnology*, 39:134–142, 2016.

Juan C Caicedo, Sam Cooper, Florian Heigwer, Scott Warchal, Peng Qiu, Csaba Molnar, Aliaksei S Vasilevich, Joseph D Barry, Harmanjit Singh Bansal, Oren Kraus, et al. Data-analysis strategies for image-based cell profiling. *Nature methods*, 14(9):849–863, 2017.

Juan C Caicedo, Claire McQuin, Allen Goodman, Shantanu Singh, and Anne E Carpenter. Weakly supervised learning of single-cell feature embeddings. In *Proceedings of the IEEE Conference on Computer Vision and Pattern Recognition*, pp. 9309–9318, 2018.

Michael Caldera, Felix Müller, Isabel Kaltenbrunner, Marco P Licciardello, Charles-Hugues Lardeau, Stefan Kubicek, and Jörg Menche. Mapping the perturbome network of cellular perturbations. *Nature Communications*, 10(1):5140, 2019.

Mathilde Caron, Hugo Touvron, Ishan Misra, Hervé Jégou, Julien Mairal, Piotr Bojanowski, and Armand Joulin. Emerging properties in self-supervised vision transformers. In *Proceedings of the IEEE/CVF international conference on computer vision*, pp. 9650–9660, 2021.

Anne E Carpenter, Thouis R Jones, Michael R Lamprecht, Colin Clarke, In Han Kang, Ola Friman, David A Guertin, Joo Han Chang, Robert A Lindquist, Jason Moffat, et al. Cellprofiler: image analysis software for identifying and quantifying cell phenotypes. *Genome biology*, 7:1–11, 2006.

Center for High Throughput Computing. Center for high throughput computing, 2006. URL `https://chtc.cs.wisc.edu/`.

CERN and OpenAIRE. Zenodo, 2013. URL `https://www.zenodo.org/`.

Srinivas Niranj Chandrasekaran, Jeanelle Ackerman, Eric Alix, D Michael Ando, John Arevalo, Melissa Bennion, Nicolas Boisseau, Adriana Borowa, Justin D Boyd, Laurent Brino, et al. Jump cell painting dataset: morphological impact of 136,000 chemical and genetic perturbations. *BioRxiv*, pp. 2023–03, 2023a.

Srinivas Niranj Chandrasekaran, Jeanelle Ackerman, Eric Alix, D Michael Ando, John Arevalo, Melissa Bennion, Nicolas Boisseau, Adriana Borowa, Justin D Boyd, Laurent Brino, et al. Jump cell painting dataset: morphological impact of 136,000 chemical and genetic perturbations. *BioRxiv*, pp. 2023–03, 2023b.

Ting Chen, Simon Kornblith, Mohammad Norouzi, and Geoffrey Hinton. A simple framework for contrastive learning of visual representations. In *International conference on machine learning*, pp. 1597–1607. PmLR, 2020.

Zitong Sam Chen, Chau Pham, Siqi Wang, Michael Doron, Nikita Moshkov, Bryan Plummer, and Juan C Caicedo. Chammi: A benchmark for channel-adaptive models in microscopy imaging. *Advances in Neural Information Processing Systems*, 36:19700–19713, 2023.

Nathan H Cho, Keith C Cheveralls, Andreas-David Brunner, Kibeom Kim, André C Michaelis, Preethi Raghavan, Hirofumi Kobayashi, Laura Savy, Jason Y Li, Hera Canaj, et al. Opencell: Endogenous tagging for the cartography of human cellular organization. *Science*, 375(6585):eabi6983, 2022.

Luca Clissa, Antonio Macaluso, Roberto Morelli, Alessandra Occhinegro, Emiliana Piscitiello, Ludovico Taddei, Marco Luppi, Roberto Amici, Matteo Cerri, Timna Hitrec, et al. Fluorescent neuronal cells v2: multi-task, multi-format annotations for deep learning in microscopy. *Scientific Data*, 11(1):184, 2024.

Ryan Conrad and Kedar Narayan. Cem500k, a large-scale heterogeneous unlabeled cellular electron microscopy image dataset for deep learning. *Elife*, 10:e65894, 2021.

MJ Cox, S Jaensch, J Van de Waeter, L Cougnaud, D Seynaeve, S Benalla, SJ Koo, I Van Den Wyngaert, JM Neefs, D Malkov, et al. Tales of 1,008 small molecules: phenomic profiling through live-cell imaging in a panel of reporter cell lines. sci. rep. 10, 13262, 2020.

MF Cuccarese, BA Earnshaw, K Heiser, B Fogelson, CT Davis, PF McLean, HB Gordon, KR Skelly, FL Weathersby, V Rodic, et al. Functional immune mapping with deep-learning enabled phenomics applied to immunomodulatory and covid-19 drug discovery. biorxiv preprint 2020; biorxiv 2020.08. 02.233064. *DOI: doi. org/10.1101/2020.08*, 2, 2020.

Kevin J Cutler, Carsen Stringer, Teresa W Lo, Luca Rappez, Nicholas Stroustrup, S Brook Peterson, Paul A Wiggins, and Joseph D Mougous. Omnipose: a high-precision morphology-independent solution for bacterial cell segmentation. *Nature methods*, 19(11): 1438–1448, 2022.

Jayme L Dahlin, Bruce K Hua, Beth E Zucconi, Shawn D Nelson Jr, Shantanu Singh, Anne E Carpenter, Jonathan H Shrimp, Evelyne Lima-Fernandes, Mathias J Wawer, Lawrence PW Chung, et al. Reference compounds for characterizing cellular injury in high-content cellular morphology assays. *Nature Communications*, 14(1):1364, 2023.

Alice V De Lorenci, Seung Eun Yi, Théo Moutakanni, Piotr Bojanowski, Juan C Caicedo, Wolfgang Maximilian Anton Pernice, et al. Scaling channel-invariant self-supervised learning. *Transactions of Machine Learning Research*, 2025.

Jia Deng, Wei Dong, Richard Socher, Li-Jia Li, Kai Li, and Li Fei-Fei. Imagenet: A large-scale hierarchical image database. In *2009 IEEE conference on computer vision and pattern recognition*, pp. 248–255. Ieee, 2009.

B Dey, R Ahmed, J Ferdous, MMU Haque, R Khatun, FE Hasan, and SN Uddin. Automated plant species identification from the stomata images using deep neural network: a study of selected mangrove and freshwater swamp forest tree species of bangladesh, ecol. inf. 75 (2023), 102128, 2023.

Minh Doan, Joseph A Sebastian, Juan C Caicedo, Stefanie Siegert, Aline Roch, Tracey R Turner, Olga Mykhailova, Ruben N Pinto, Claire McQuin, Allen Goodman, et al. Objective assessment of stored blood quality by deep learning. *Proceedings of the National Academy of Sciences*, 117(35):21381–21390, 2020.

Carsten Doil, Niels Mailand, Simon Bekker-Jensen, Patrice Menard, Dorthe Helena Larsen, Rainer Pepperkok, Jan Ellenberg, Stephanie Panier, Daniel Durocher, Jiri Bartek, et al. Rnf168 binds and amplifies ubiquitin conjugates on damaged chromosomes to allow accumulation of repair proteins. *Cell*, 136(3):435–446, 2009.

Michael Doron, Théo Moutakanni, Zitong S Chen, Nikita Moshkov, Mathilde Caron, Hugo Touvron, Piotr Bojanowski, Wolfgang M Pernice, and Juan C Caicedo. Unbiased single-cell morphology with self-supervised vision transformers. *bioRxiv*, 2023.

Christoffer Edlund, Timothy R Jackson, Nabeel Khalid, Nicola Bevan, Timothy Dale, Andreas Dengel, Sheraz Ahmed, Johan Trygg, and Rickard Sjögren. Livecell—a large-scale dataset for label-free live cell segmentation. *Nature methods*, 18(9):1038–1045, 2021.

B Ellinger, D Bojkova, A Zaliani, J Cinatl, C Claussen, S Westhaus, et al. A sars-cov-2 cytopathicity dataset generated by high-content screening of a large drug repurposing collection. sci data [internet], 2021.

Elsevier. Mendeley data, 2025. `https://data.mendeley.com/` [Accessed: May/2025].

Harry Fischl, David McManus, Roel Oldenkamp, Lothar Schermelleh, Jane Mellor, Aarti Jagannath, and André Furger. Cold-induced chromatin compaction and nuclear retention of clock mrnas resets the circadian rhythm. *The EMBO journal*, 39(22):e105604, 2020.

Ka-wing Fong, Yujing Li, Wenqi Wang, Wenbin Ma, Kunpeng Li, Robert Z Qi, Dan Liu, Zhou Songyang, and Junjie Chen. Whole-genome screening identifies proteins localized to distinct nuclear bodies. *Journal of Cell Biology*, 203(1):149–164, 2013.

Florian Fuchs, Gregoire Pau, Dominique Kranz, Oleg Sklyar, Christoph Budjan, Sandra Steinbrink, Thomas Horn, Angelika Pedal, Wolfgang Huber, and Michael Boutros. Clustering phenotype populations by genome-wide rnai and multiparametric imaging. *Molecular systems biology*, 6(1):370, 2010.

Fanny Georgi, Fabien Kuttler, Luca Murer, Vardan Andriasyan, Robert Witte, Artur Yakimovich, Gerardo Turcatti, and Urs F Greber. A high-content image-based drug screen of clinical compounds against cell transmission of adenovirus. *Scientific data*, 7(1):265, 2020.

Yolla German, Loan Vulliard, Anton Kamnev, Laurène Pfajfer, Jakob Huemer, Anna-Katharina Mautner, Aude Rubio, Artem Kalinichenko, Kaan Boztug, Audrey Ferrand, et al. Morphological profiling of human t and nk lymphocytes by high-content cell imaging. *Cell Reports*, 36(1), 2021.

Veronika Graml, Xenia Studera, Jonathan LD Lawson, Anatole Chessel, Marco Geymonat, Miriam Bortfeld-Miller, Thomas Walter, Laura Wagstaff, Eugenia Piddini, and Rafael E Carazo-Salas. A genomic multiprocess survey of machineries that control and link cell shape, microtubule organization, and cell-cycle progression. *Developmental cell*, 31(2): 227–239, 2014.

Ankit Gupta, Zoe Wefers, Konstantin Kahnert, Jan N Hansen, Will Leineweber, Anthony Cesnik, Dan Lu, Ulrika Axelsson, Frederic Ballllosera Navarro, Theofanis Karaletsos, et al. Subcell: Vision foundation models for microscopy capture single-cell biology. *bioRxiv*, pp. 2024–12, 2024.

Matthew Hartley, Gerard J Kleywegt, Ardan Patwardhan, Ugis Sarkans, Jason R Swedlow, and Alvis Brazma. The bioimage archive–building a home for life-sciences microscopy data. *Journal of Molecular Biology*, 434(11):167505, 2022.

Kaiming He, Xinlei Chen, Saining Xie, Yanghao Li, Piotr Dollár, and Ross Girshick. Masked autoencoders are scalable vision learners. In *Proceedings of the IEEE/CVF conference on computer vision and pattern recognition*, pp. 16000–16009, 2022.

Katie Heiser, Peter F McLean, Chadwick T Davis, Ben Fogelson, Hannah B Gordon, Pamela Jacobson, Brett Hurst, Ben Miller, Ronald W Alfa, Berton A Earnshaw, et al. Identification of potential treatments for covid-19 through artificial intelligence-enabled phenomic analysis of human cells infected with sars-cov-2. *BioRxiv*, pp. 2020–04, 2020.

Jean-Karim Hériché, Jon G Lees, Ian Morilla, Thomas Walter, Boryana Petrova, M Julia Roberti, M Julius Hossain, Priit Adler, José M Fernández, Martin Krallinger, et al. Integration of biological data by kernels on graph nodes allows prediction of new genes involved in mitotic chromosome condensation. *Molecular biology of the cell*, 25(16):2522–2536, 2014.

Brandon Ho, Raphael Loll-Krippleber, Nikko P Torres, Andreas Cuny, Fabian Rudolf, and Grant W Brown. Phenotypic heterogeneity in the dna replication stress response revealed by quantitative protein dynamics measurements. *BioRxiv*, pp. 2022–06, 2022.

Brandon Ho, Ethan J Sanford, Raphael Loll-Krippleber, Nikko P Torres, Marcus B Smolka, and Grant W Brown. Mec1-independent activation of the rad53 checkpoint kinase revealed by quantitative analysis of protein localization dynamics. *Elife*, 12:e82483, 2023.

Stanley Bryan Z Hua, Alex X Lu, and Alan M Moses. Cytoimagenet: A large-scale pretraining dataset for bioimage transfer learning. *arXiv preprint arXiv:2111.11646*, 2021.

Andrii Iudin, Paul K Korir, Sriram Somasundharam, Simone Weyand, Cesare Cattavitello, Neli Fonseca, Osman Salih, Gerard J Kleywegt, and Ardan Patwardhan. Empiar: the electron microscopy public image archive. *Nucleic Acids Research*, 51(D1):D1503–D1511, 2023.

Aaron Jaech, Adam Kalai, Adam Lerer, Adam Richardson, Ahmed El-Kishky, Aiden Low, Alec Helyar, Aleksander Madry, Alex Beutel, Alex Carney, et al. Openai o1 system card. *arXiv preprint arXiv:2412.16720*, 2024.

Rebecca A Jones, Matthew J Renshaw, and David J Barry. Automated staging of zebrafish embryos with deep learning. *Life Science Alliance*, 7(1), 2024.

Kaggle. Kaggle, 2025. `https://www.kaggle.com/` [Accessed: May/2025].

Alexandr A Kalinin, John Arevalo, Erik Serrano, Loan Vulliard, Hillary Tsang, Michael Bornholdt, Alán F Muñoz, Suganya Sivagurunathan, Bartek Rajwa, Anne E Carpenter, et al. A versatile information retrieval framework for evaluating profile strength and similarity. *Nature Communications*, 16(1):5181, 2025.

Byunguk Kang, Michael Murphy, Christopher W Ng, Matthew Joseph Leventhal, Nhan Huynh, Egun Im, Serwah Danquah, David E Housman, Ralda Nehme, Samouil L Farhi, et al. Cellfie: Integrating pathway discovery with pooled profiling of perturbations uncovers pathways of huntington's disease, including genetic modifiers of neuronal development and morphology. *bioRxiv*, 2025.

Carly Kempster, George Butler, Elina Kuznecova, Kirk A Taylor, Neline Kriek, Gemma Little, Marcin A Sowa, Tanya Sage, Louise J Johnson, Jonathan M Gibbins, et al. Fully automated platelet differential interference contrast image analysis via deep learning. *Scientific reports*, 12(1):4614, 2022.

Kian Kenyon-Dean, Zitong Jerry Wang, John Urbanik, Konstantin Donhauser, Jason Hartford, Saber Saberian, Nil Sahin, Ihab Bendidi, Safiye Celik, Marta Fay, et al. Vitally consistent: Scaling biological representation learning for cell microscopy. *arXiv preprint arXiv:2411.02572*, 2024.

Payam Khoshkenar, Emily Lowry, and Amir Mitchell. Rapid signaling reactivation after targeted braf inhibition predicts the proliferation of individual melanoma cells from an isogenic population. *Scientific Reports*, 11(1):15473, 2021.

Prannay Khosla, Piotr Teterwak, Chen Wang, Aaron Sarna, Yonglong Tian, Phillip Isola, Aaron Maschinot, Ce Liu, and Dilip Krishnan. Supervised contrastive learning. *Advances in neural information processing systems*, 33:18661–18673, 2020.

Vladislav Kim, Nikolaos Adaloglou, Marc Osterland, Flavio M Morelli, Marah Halawa, Tim König, David Gnutt, and Paula A Marin Zapata. Self-supervision advances morphological profiling by unlocking powerful image representations. *Scientific Reports*, 15(1):4876, 2025.

Esmee Koedoot, Michiel Fokkelman, Vasiliki-Maria Rogkoti, Marcel Smid, Iris van de Sandt, Hans de Bont, Chantal Pont, Janna E Klip, Steven Wink, Mieke A Timmermans, et al. Uncovering the signaling landscape controlling breast cancer cell migration identifies novel metastasis driver genes. *Nature communications*, 10(1):2983, 2019.

Krisztian Koos, József Molnár, Lóránd Kelemen, Gábor Tamás, and Peter Horvath. Dic image reconstruction using an energy minimization framework to visualize optical path length distribution. *Scientific reports*, 6(1):30420, 2016.

Oren Kraus, Kian Kenyon-Dean, Saber Saberian, Maryam Fallah, Peter McLean, Jess Leung, Vasudev Sharma, Ayla Khan, Jia Balakrishnan, Safiye Celik, et al. Masked autoencoders for microscopy are scalable learners of cellular biology. In *Proceedings of the IEEE/CVF Conference on Computer Vision and Pattern Recognition*, pp. 11757–11768, 2024.

Florian Kromp, Eva Bozsaky, Fikret Rifatbegovic, Lukas Fischer, Magdalena Ambros, Maria Berneder, Tamara Weiss, Daria Lazic, Wolfgang Dörr, Allan Hanbury, et al. An annotated fluorescence image dataset for training nuclear segmentation methods. *Scientific Data*, 7 (1):262, 2020.

Trang Le, Casper F Winsnes, Ulrika Axelsson, Hao Xu, Jayasankar Mohanakrishnan Kaimal, Diana Mahdessian, Shubin Dai, Ilya S Makarov, Vladislav Ostankovich, Yang Xu, et al. Analysis of the human protein atlas weakly supervised single-cell classification competition. *Nature methods*, 19(10):1221–1229, 2022.

Elena Ledesma-Fernández and Peter H Thorpe. Fluorescent foci quantitation for high-throughput analysis. *Journal of biological methods*, 2(2):e22, 2015.

Wenyi Lian, Joakim Lindblad, Patrick Micke, and Nataša Sladoje. Isolated channel vision transformers: From single-channel pretraining to multi-channel finetuning. *arXiv preprint arXiv:2503.09826*, 2025.

Miron Livny, Jim Basney, Rajesh Raman, Todd Tannenbaum, et al. Mechanisms for high throughput computing. *SPEEDUP journal*, 11(1):36–40, 1997.

Vebjorn Ljosa, Katherine L Sokolnicki, and Anne E Carpenter. Annotated high-throughput microscopy image sets for validation. *Nature methods*, 9(7):637, 2012.

Vebjorn Ljosa, Peter D Caie, Rob Ter Horst, Katherine L Sokolnicki, Emma L Jenkins, Sandeep Daya, Mark E Roberts, Thouis R Jones, Shantanu Singh, Auguste Genovesio, et al. Comparison of methods for image-based profiling of cellular morphological responses to small-molecule treatment. *Journal of biomolecular screening*, 18(10):1321–1329, 2013.

Gendarme Mathieu, El Debs Bachir, et al. Brifiseg: a deep learning-based method for semantic and instance segmentation of nuclei in brightfield images. *arXiv preprint arXiv:2211.03072*, 2022.

Ezequiel Miron, Roel Oldenkamp, Jill M Brown, David MS Pinto, C Shan Xu, Ana R Faria, Haitham A Shaban, James DP Rhodes, Cassandravictoria Innocent, Sara De Ornellas, et al. Chromatin arranges in chains of mesoscale domains with nanoscale functional topography independent of cohesin. *Science advances*, 6(39):eaba8811, 2020.

Erick Moen, Dylan Bannon, Takamasa Kudo, William Graf, Markus Covert, and David Van Valen. Deep learning for cellular image analysis. *Nature methods*, 16(12):1233–1246, 2019.

Flavio M Morelli, Vladislav Kim, Franziska Hecker, Sven Geibel, and Paula A Marín Zapata. unidino: Assay-independent feature extraction for fluorescence microscopy images. *Computational and Structural Biotechnology Journal*, 27:928–936, 2025.

Nikita Moshkov, Michael Bornholdt, Santiago Benoit, Matthew Smith, Claire McQuin, Allen Goodman, Rebecca A Senft, Yu Han, Mehrtash Babadi, Peter Horvath, et al. Learning representations for image-based profiling of perturbations. *Nature communications*, 15 (1):1594, 2024.

Ana Mota, Maud Schweitzer, Erik Wernersson, Nicola Crosetto, and Magda Bienko. Simultaneous visualization of dna loci in single cells by combinatorial multi-color ifish. *Scientific Data*, 9(1):47, 2022.

Micha Müller, Merve Avar, Daniel Heinzer, Marc Emmenegger, Adriano Aguzzi, Lucas Pelkmans, and Scott Berry. High content genome-wide sirna screen to investigate the coordination of cell size and rna production. *Scientific Data*, 8(1):162, 2021.

Beate Neumann, Thomas Walter, Jean-Karim Hériché, Jutta Bulkescher, Holger Erfle, Christian Conrad, Phill Rogers, Ina Poser, Michael Held, Urban Liebel, et al. Phenotypic profiling of the human genome by time-lapse microscopy reveals cell division genes. *Nature*, 464(7289):721–727, 2010.

Alma Mater Studiorum University of Bologna. Ams acta, 2025. `https://amsacta.unibo.it/` [Accessed: May/2025].

University of Reading. University of reading research data archive, 2025. `https://researchdata.reading.ac.uk/` [Accessed: May/2025].

D Olszewski, F Georgi, L Murer, V Andriasyan, F Kuttler, A Petkidis, R Witte, A Yakimovich, L Fischer, A Rozanova, et al. High-content, arrayed compound screens with rhinovirus, influenza a virus and herpes simplex virus infections. sci data 9: 610, 2022.

Maxime Oquab, Timothée Darcet, Théo Moutakanni, Huy Vo, Marc Szafraniec, Vasil Khalidov, Pierre Fernandez, Daniel Haziza, Francisco Massa, Alaaeldin El-Nouby, et al. Dinov2: Learning robust visual features without supervision. *arXiv preprint arXiv:2304.07193*, 2023.

OSF. Osf, 2025. `https://osf.io/` [Accessed: May/2025].

Shotaro Otsuka, Jeremy OB Tempkin, Wanlu Zhang, Antonio Z Politi, Arina Rybina, M Julius Hossain, Moritz Kueblbeck, Andrea Callegari, Birgit Koch, Natalia Rosalia Morero, et al. A quantitative map of nuclear pore assembly reveals two distinct mechanisms. *Nature*, 613(7944):575–581, 2023.

Wei Ouyang, Casper F Winsnes, Martin Hjelmare, Anthony J Cesnik, Lovisa Åkesson, Hao Xu, Devin P Sullivan, Shubin Dai, Jun Lan, Park Jinmo, et al. Analysis of the human protein atlas image classification competition. *Nature methods*, 16(12):1254–1261, 2019.

Marius Pachitariu and Carsen Stringer. Cellpose 2.0: how to train your own model. *Nature methods*, 19(12):1634–1641, 2022.

Patricia Pascual-Vargas, Samuel Cooper, Julia Sero, Vicky Bousgouni, Mar Arias-Garcia, and Chris Bakal. Rnai screens for rho gtpase regulators of cell shape and yap/taz localisation in triple negative breast cancer. *Scientific data*, 4(1):1–13, 2017.

Nick Pawlowski, Juan C Caicedo, Shantanu Singh, Anne E Carpenter, and Amos Storkey. Automating morphological profiling with generic deep convolutional networks. *BioRxiv*, pp. 085118, 2016.

Chau Pham and Bryan Plummer. Enhancing feature diversity boosts channel-adaptive vision transformers. *Advances in Neural Information Processing Systems*, 37:89782–89805, 2024.

Chau Pham, Juan C Caicedo, and Bryan A Plummer. Cha-maevit: Unifying channel-aware masked autoencoders and multi-channel vision transformers for improved cross-channel learning. *arXiv preprint arXiv:2503.19331*, 2025.

Aditya Pratapa, Michael Doron, and Juan C Caicedo. Image-based cell phenotyping with deep learning. *Current opinion in chemical biology*, 65:9–17, 2021.

Recursion. Rxrx, 2025. `https://www.rxrx.ai/datasets` [Accessed: May/2025].

Mohammad Hossein Rohban, Shantanu Singh, Xiaoyun Wu, Julia B Berthet, Mark-Anthony Bray, Yashaswi Shrestha, Xaralabos Varelas, Jesse S Boehm, and Anne E Carpenter. Systematic morphological profiling of human gene and allele function via cell painting. *Elife*, 6:e24060, 2017.

Jennifer L Rohn, David Sims, Tao Liu, Marina Fedorova, Frieder Schöck, Joseph Dopie, Maria K Vartiainen, Amy A Kiger, Norbert Perrimon, and Buzz Baum. Comparative rnai screening identifies a conserved core metazoan actinome by phenotype. *Journal of Cell Biology*, 194(5):789–805, 2011.

Christopher Schmied, Michael S Nelson, Sergiy Avilov, Gert-Jan Bakker, Cristina Bertocchi, Johanna Bischof, Ulrike Boehm, Jan Brocher, Mariana T Carvalho, Catalin Chiritescu, et al. Community-developed checklists for publishing images and image analyses. *Nature Methods*, 21(2):170–181, 2024.

Wiebke Schormann, Santosh Hariharan, and David W Andrews. A reference library for assigning protein subcellular localizations by image-based machine learning. *Journal of Cell Biology*, 219(3):e201904090, 2020.

Christoph Schuhmann, Romain Beaumont, Richard Vencu, Cade Gordon, Ross Wightman, Mehdi Cherti, Theo Coombes, Aarush Katta, Clayton Mullis, Mitchell Wortsman, et al. Laion-5b: An open large-scale dataset for training next generation image-text models. *Advances in neural information processing systems*, 35:25278–25294, 2022.

Mischa Schwendy, Ronald E Unger, and Sapun H Parekh. Evican—a balanced dataset for algorithm development in cell and nucleus segmentation. *Bioinformatics*, 36(12): 3863–3870, 2020.

Julia E Sero and Chris Bakal. Multiparametric analysis of cell shape demonstrates that β-pix directly couples yap activation to extracellular matrix adhesion. *Cell systems*, 4(1): 84–96, 2017.

Erik Serrano, Srinivas Niranj Chandrasekaran, Dave Bunten, Kenneth I Brewer, Jenna Tomkinson, Roshan Kern, Michael Bornholdt, Stephen J Fleming, Ruifan Pei, John Arevalo, Hillary Tsang, Vincent Rubinetti, Callum Tromans-Coia, Tim Becker, Erin Weisbart, Charlotte Bunne, Alexandr A Kalinin, Rebecca Senft, Stephen J Taylor, Nasim Jamali, Adeniyi Adeboye, Hamdah Shafqat Abbasi, Allen Goodman, Juan C Caicedo, Anne E Carpenter, Beth A Cimini, Shantanu Singh, and Gregory P Way. Reproducible image-based profiling with pycytominer. *Nat. Methods*, 22(4):677–680, April 2025.

Oriane Siméoni, Huy V Vo, Maximilian Seitzer, Federico Baldassarre, Maxime Oquab, Cijo Jose, Vasil Khalidov, Marc Szafraniec, Seungeun Yi, Michaël Ramamonjisoa, et al. Dinov3. *arXiv preprint arXiv:2508.10104*, 2025.

Jeremy C Simpson, Brigitte Joggerst, Vibor Laketa, Fatima Verissimo, Cihan Cetin, Holger Erfle, Mariana G Bexiga, Vasanth R Singan, Jean-Karim Hériché, Beate Neumann, et al. Genome-wide rnai screening identifies human proteins with a regulatory function in the early secretory pathway. *Nature cell biology*, 14(7):764–774, 2012.

Jatinder Singh. Figshare. *Journal of pharmacology & pharmacotherapeutics*, 2(2):138, 2011.

Max Planck Society. Edmond, 2025. `https://edmond.mpg.de/` [Accessed: May/2025].

Christoph Spahn, Estibaliz Gómez-de Mariscal, Romain F Laine, Pedro M Pereira, Lucas von Chamier, Mia Conduit, Mariana G Pinho, Guillaume Jacquemet, Séamus Holden, Mike Heilemann, et al. Deepbacs for multi-task bacterial image analysis using open-source deep learning approaches. *Communications Biology*, 5(1):688, 2022.

Tharan Srikumar, Megan C Lewicki, Michael Costanzo, Johnny M Tkach, Harm van Bakel, Kyle Tsui, Erica S Johnson, Grant W Brown, Brenda J Andrews, Charles Boone, et al. Global analysis of sumo chain function reveals multiple roles in chromatin regulation. *Journal of Cell Biology*, 201(1):145–163, 2013.

Charlotte Stadler, Martin Hjelmare, Beate Neumann, Kalle Jonasson, Rainer Pepperkok, Mathias Uhlén, and Emma Lundberg. Systematic validation of antibody binding and protein subcellular localization using sirna and confocal microscopy. *Journal of proteomics*, 75(7):2236–2251, 2012.

Lovorka Stojic, Aaron TL Lun, Patrice Mascalchi, Christina Ernst, Aisling M Redmond, Jasmin Mangei, Alexis R Barr, Vicky Bousgouni, Chris Bakal, John C Marioni, et al. A high-content rnai screen reveals multiple roles for long noncoding rnas in cell division. *Nature communications*, 11(1):1851, 2020.

Carsen Stringer, Tim Wang, Michalis Michaelos, and Marius Pachitariu. Cellpose: a generalist algorithm for cellular segmentation. *Nature methods*, 18(1):100–106, 2021.

Tim Stuart, Andrew Butler, Paul Hoffman, Christoph Hafemeister, Efthymia Papalexi, William M Mauck, Yuhan Hao, Marlon Stoeckius, Peter Smibert, and Rahul Satija. Comprehensive integration of single-cell data. *cell*, 177(7):1888–1902, 2019.

Ilida Suleymanova, Tamas Balassa, Sushil Tripathi, Csaba Molnar, Mart Saarma, Yulia Sidorova, and Peter Horvath. A deep convolutional neural network approach for astrocyte detection. *Scientific reports*, 8(1):12878, 2018.

M Sypetkowski, M Rezanejad, S Saberian, O Kraus, J Urbanik, J Taylor, B Mabey, M Victors, J Yosinski, AR Sereshkeh, et al. Rxrx1: a dataset for evaluating experimental batch correction methods, january 2023. *arXiv preprint arXiv:2301.05768*, 2023.

Ole Tange. Gnu parallel 20241222 ('bashar'), December 2024. URL `https://doi.org/10.5281/zenodo.14550073`. GNU Parallel is a general parallelizer to run multiple serial command line programs in parallel without changing them.

Vajira Thambawita, Steven A Hicks, Andrea M Storås, Thu Nguyen, Jorunn M Andersen, Oliwia Witczak, Trine B Haugen, Hugo L Hammer, Pål Halvorsen, and Michael A Riegler. Visem-tracking, a human spermatozoa tracking dataset. *Scientific data*, 10(1):260, 2023.

Peter J Thul, Lovisa Åkesson, Mikaela Wiking, Diana Mahdessian, Aikaterini Geladaki, Hammou Ait Blal, Tove Alm, Anna Asplund, Lars Björk, Lisa M Breckels, et al. A subcellular map of the human proteome. *Science*, 356(6340):eaal3321, 2017.

Christopher P Toret, Michael V D'Ambrosio, Ronald D Vale, Michael A Simon, and W James Nelson. A genome-wide screen identifies conserved protein hubs required for cadherin-mediated cell–cell adhesion. *Journal of Cell Biology*, 204(2):265–279, 2014.

Elena Y Trizna, Aleksandr M Sinitca, Asya I Lyanova, Diana R Baidamshina, Pavel V Zelenikhin, Dmitrii I Kaplun, Airat R Kayumov, and Mikhail I Bogachev. Brightfield vs fluorescent staining dataset–a test bed image set for machine learning based virtual staining. *Scientific Data*, 10(1):160, 2023.

Matheus P Viana, Jianxu Chen, Theo A Knijnenburg, Ritvik Vasan, Calysta Yan, Joy E Arakaki, Matte Bailey, Ben Berry, Antoine Borensztejn, Eva M Brown, et al. Integrated intracellular organization and its variations in human ips cells. *Nature*, 613(7943):345–354, 2023.

Alessandra Vigilante, Anna Laddach, Nathalie Moens, Ruta Meleckyte, Andreas Leha, Arsham Ghahramani, Oliver J Culley, Annie Kathuria, Chloe Hurling, Alice Vickers, et al. Identifying extrinsic versus intrinsic drivers of variation in cell behavior in human ipsc lines from healthy donors. *Cell reports*, 26(8):2078–2087, 2019.

Huy V Vo, Vasil Khalidov, Timothée Darcet, Théo Moutakanni, Nikita Smetanin, Marc Szafraniec, Hugo Touvron, Camille Couprie, Maxime Oquab, Armand Joulin, et al. Automatic data curation for self-supervised learning: A clustering-based approach. *arXiv preprint arXiv:2405.15613*, 2024.

Giovanni Volpe, Carolina Wählby, Lei Tian, Michael Hecht, Artur Yakimovich, Kristina Monakhova, Laura Waller, Ivo F Sbalzarini, Christopher A Metzler, Mingyang Xie, et al. Roadmap on deep learning for microscopy. *ArXiv*, pp. arXiv–2303, 2023.

Gregory P Way, Maria Kost-Alimova, Tsukasa Shibue, William F Harrington, Stanley Gill, Federica Piccioni, Tim Becker, Hamdah Shafqat-Abbasi, William C Hahn, Anne E Carpenter, et al. Predicting cell health phenotypes using image-based morphology profiling. *Molecular biology of the cell*, 32(9):995–1005, 2021.

Erin Weisbart, Ankur Kumar, John Arevalo, Anne E Carpenter, Beth A Cimini, and Shantanu Singh. Cell painting gallery: an open resource for image-based profiling. *Nature Methods*, 21(10):1775–1777, 2024.

Eleanor Williams, Josh Moore, Simon W Li, Gabriella Rustici, Aleksandra Tarkowska, Anatole Chessel, Simone Leo, Bálint Antal, Richard K Ferguson, Ugis Sarkans, et al. Image data resource: a bioimage data integration and publication platform. *Nature methods*, 14 (8):775–781, 2017.

Fuyong Xing, Yuanpu Xie, Hai Su, Fujun Liu, and Lin Yang. Deep learning in microscopy image analysis: A survey. *IEEE transactions on neural networks and learning systems*, 29(10):4550–4568, 2017.

Dejin Xun, Rui Wang, Xingcai Zhang, and Yi Wang. Microsnoop: A generalist tool for microscopy image representation. *The Innovation*, 5(1), 2024.

Artur Yakimovich and Evgeniy Galimov. A tandem segmentation-classification approach for the localization of morphological predictors of c. elegans lifespan and motility. *BioRxiv*, pp. 2021–05, 2021.

Chi Zhang, Hao Jiang, Weihuang Liu, Junyi Li, Shiming Tang, Mario Juhas, and Yang Zhang. Correction of out-of-focus microscopic images by deep learning. *Computational and Structural Biotechnology Journal*, 20:1957–1966, 2022.

Xin Zheng, Yong Wang, Guoyou Wang, and Jianguo Liu. Fast and robust segmentation of white blood cell images by self-supervised learning. *Micron*, 107:55–71, 2018.

A Dataset

The CHAMMI-75 dataset contains two versions for pre-training: a small dataset for development and ablation studies, and a large dataset for scaling models. Table A3 reports the number of images in each set.

Table A3: Number of multi-channel images in the small and large pretraining sets

Set	# Single Channel Images	# Multi-Channel Images
Small	1,679,765	560,558
Large	8,029,583	2,849,483

A.1 Data Preparation

Before sampling and data curation, all the data from the original 75 studies was downloaded to our local servers in their original TIFF/OME 16-bit formats. We used a high-throughput computing cluster (Center for High Throughput Computing, 2006), Condor workflows (Livny et al., 1997), and GNU Parallel (Tange, 2024) for pre-processing and standardization of these datasets, bringing them down to ∼50TB of compressed images. First, we decoded the original image format (e.g., TIFF, flex, etc) and separated individual channels, individual z-planes, and individual temporal frames into separate files. Next, we standardized pixel depth from the original (e.g., 12 or 16 bits) to 8 bits after rescaling illumination values. Images intensities were normalized between 0 and 255 after trimming the tail end distributions of the initial histogram at the 0.1% and 99.9% percentiles. Finally, each single file was independently stored in PNG format with lossless compression, resulting in ∼42M individual channel files. Note that no spatial rescaling or cropping was used to reduce storage size — images in our dataset preserve their original resolution.

A.2 Dataset Curation

3D sampling. Seven of the 75 studies involve imaging data acquired in three dimensions, i.e., z-planes recorded at various depths. Given that our focus is 2D imaging, we sampled 20% of the z-planes from the central region of the 3D stack. This follows two observations: first, images in the extremes of the stack appear to be empty or out of focus in most cases. Second, z-planes from the same 3D stack are highly correlated and may not bring new information from the 2D perspective. After applying this filtering, we reduced the number of multi-channel images from 26.7M to 24.2M. A4 reports the sampling information for all the 3D studies.

Table A4: 3D Sampling Information for Multi-Channel Images

Dataset Name	Multi-Channel Images		
	After	Before	Ratio Preserved
idr0001	741,960	2,374,272	0.3125
idr0011	39,890	167,551	0.2381
idr0086	16,705	76,851	0.2174
idr0089	8,857	40,565	0.2183
idr0115	138,035	579,747	0.2381
idr0120	75,828	192,908	0.3931
idr0123	3,394	13,342	0.2544
wtc0001	39,294	117,882	0.3333

Temporal sampling. Nine of the 75 studies involve time-lapse imaging, i.e., images acquired through time. In live microscopy, the camera does not move and the cells do not move too quickly, resulting in highly correlated 2D frames. Following the same intuitions from 3D sampling, we sampled a fraction of the frames by defining evenly distributed time points in a given sequence. With this, we reduced the number of multi-channel images from 24.2M to 6.8M. A5 reports the sampling information for all the temporal studies.

Table A5: Temporal Sampling of Studies for Multi-Channel Images

Dataset Name	Multi-Channel Images		
	After	Before	Percent Preserved
idr0002	43,392	386,884	0.1122
idr0011	39,890	39,890	1
idr0013	959,795	17,848,117	0.0538
idr0115	14,815	138,035	0.1073
nidr0003	16,699	33,403	0.4999
nidr0020	14,685	29,370	0.5

Control-based sampling. The majority of studies in the collection involve experiments with control conditions used to compare against treatments. Control samples are usually abundant and replicated multiple times to improve the ability to make meaningful comparisons. To reduce redundancy, we sampled a fraction of the control images to balance its representation with respect to treatment samples. This reduced the number of multi-channel images from 6.8M to 5.9M.

Intensity filtering. The pixel intensity statistics of microscopy images tend to have a low mean and a long tail distribution. We filtered channels whose mean pixel intensity is too dark with respect to the distribution of all channels in the same study, under the assumption that these images are mostly empty FoV or have too small or too few interesting objects.

A.3 Metadata parsing

The resulting metadata file is useful to understand the distribution of images and to sample a representative subset. Figure 4 illustrates the diversity of images after selection and sampling according to a few relevant annotations, which could be leveraged for learning. Importantly, while there are many types of images represented, the specific subgroups in the training set are sparse and have long-tail distributions (Fig. 4b). This is a known challenge of real world data and an opportunity to investigate robust learning strategies despite the natural biases. Also, note that the original sources may not have all the information of the 22 columns that we tried to parse, due to lack of standards for imaging metadata (Schmied et al., 2024). Therefore, the final metadata file may have missing information for some studies.

Techniques Used to Reduce the Number of Reagents in the Metadata After merging all metadata sources the resulting file contained 145k reagents, which were reduced to 92k using multiple alignment techniques. We performed metadata harmonization to address heterogeneous identifiers and naming conventions in the candidate list. Using a programmatic gene-ID mapping step (mygene) we mapped ENSEMBL identifiers to HGNC symbols and removed records that were duplicates by virtue of having both identifiers; this eliminated 16,029 ENSEMBL-only redundancies and reduced the working set to 114,748 reagents. We then applied a sequence of regex- and rule-based sanitization passes: we discarded tokens of two characters or fewer, removed purely numeric tokens of three characters or fewer, and normalized hyphenation to collapse format mismatches (for example, MK2206 versus MK-2206) while explicitly preserving legitimate hyphens that encode stereochemistry, numbered loci distinctions (gene1-1 versus gene11), and organism-specific conventions (for example, fly/worm par-1 versus human PAR1). We also stripped timestamp-like experimental annotations appended to gene symbols (for example, HU-90-min-ILK6) and, when a canonical symbol existed elsewhere in the list, removed the annotated variant entirely. We also used some databases such as Flybase, and Pombase datasets to rename Drosophila and Yeast related genes.

Ground Truth Extraction for IDR Studies We developed a reproducible, meta-data-paper pipeline to adjudicate "hit" versus "no hit" labels for candidate metadata reagents using the content present in each paper's reconstructed text, tables, and machine-generated figure descriptions. A dataset-specific prompt encodes the inclusion criteria for what constitutes a hit in that study.

The pipeline begins by loading the reconstructed text for a selected study. If image links are present in the text, we apply a two-stage figure augmentation pass using OpenAI's o1 model (Jaech et al., 2024). First, we download each image and produce a transcription that captures the image, visible labels and legend text. Second, we use the figure transcription to summarize roles, interactions, conditions, and quantitative readouts described in the figure. For each image, the URL in the text is replaced with the generated description so that subsequent steps operate on a text representation that incorporates figure content.

Candidate entity construction is metadata-driven. We read the study's reagent or gene list line-by-line and derive name variants by lowercasing, extracting parenthetical synonyms, and stripping common suffix words to produce base names. We compile a word-bounded regular-expression union of all variants, exclude very short tokens and a small stoplist to reduce spurious matches, and scan the augmented text to recover a de-duplicated set of candidates that are explicitly mentioned in the paper. Because candidates originate from the metadata list and are matched with word boundaries, we limit substring bleed (for example, avoiding matches of "ER" within "ERK").

Hit adjudication is performed by invoking paper specific "hit" definitions for each candidate against the full augmented text under a text-only evidence policy. The adjudicator, OpenAI's o1 model, must both assert whether the candidate meets the inclusion criteria and return a concise rationale together with a short, verbatim in-text snippet that substantiates the decision; labels without a snippet do not qualify as positive.

Inclusion criteria are encoded per dataset to reflect the study's stated endpoints. For IDR0017 specifically, a hit is a reagent that exhibits interaction activity with any screened cell line. In all cases, external knowledge is disallowed and every positive must be justified by an in-paper snippet. Outputs consist of a per-reagent record written to a study-specific text file that captures the final label, a brief rationale, and a snippet of at most two sentences that provides the evidentiary anchor. We additionally persist the full processing log, the augmented text file where applicable, and a JSON file with per-figure transcriptions and relationship summaries. Each record includes provenance fields such as the paper identifier, the exact matched string for the entity, model name and version, timestamps, and prompt versions to facilitate audits and downstream benchmarking.

A.4 Metadata Columns and Descriptions

Our metadata fields are divided into six different groups, where each group corresponds to a particular type of experiment. The metadata comes in six major groups: experiment, biology, imaging, microscopy, geometry, and storage information. Each record in the metadata file points to a single channel file. The metadata is designed to facilitate grouping of channel files according to the categories described before. For each category, we have several metadata columns described below. If the information for an image is missing or not known, the corresponding value will be labeled with the string "unknown". We try not to leave NaN or empty strings in the metadata file. If you see something, say something. A9 contains visualization of the six groups of metadata and the 22 fields present in the metadata.

We are going to provide a detailed list with descriptions for all the different columns present in the metadata:

1. **experiment.study**: Identifier of the study.
2. **experiment.plate**: Plate where the image was acquired. If images come from another format (not plate-based), this identifier can indicate a major group of experimental arrangements in the study.
3. **experiment.well**: Well position within the plate. The format of letter and number is preferred, but this is flexible.
4. **experiment.reagent**: Identifier or name of the treatment or reagent used to treat the cells. In many cases, this is a gene name, a compound name, or a protein

name, while in other cases it may reflect other experimental interventions (e.g., temperature).

5. **experiment.control**: Whether the image comes from a control well or not, and what type of control they may be, for example, positive or negative control. If not a control, use the string "no".
6. **biology.organism**: Name of the organism where the cells come from. For example, humans, mice, plants, etc.
7. **biology.cell_line**: Name of the cell line. Many cell lines have well-known names (such as HeLa), other cell lines are from primary patients and have anonymized codes, and others are from genetically modified organisms.
8. **biology.cell_type**: The functional type of cell, regardless of the cell line. Examples include neurons, red blood cells, cancer cells, pancreatic cells, etc.
9. **imaging.multi_channel_id**: This is the field that ties together multiple channels. It is a consecutive number from the original database concatenated with the study number. A unique `multi_channel_id` connects the channels of an image.
10. **imaging.panel**: Names and dyes of the channels used to create the image. This gives context for where the observed channel file comes from. Example: "DNA, protein, cytoplasm".
11. **imaging.channel**: Numeric value of the channel according to the panel. This value is one-based.
12. **imaging.channel_type**: Biological compartment of the cell that is visible in the channel. This is a list of standardized values that include: nucleus, cell body, bright-field, etc.
13. **microscopy.type**: Name of the type of microscopy used for acquisition of the channel file. Examples include: fluorescence, bright-field, confocal, cryoEM, etc.
14. **microscopy.magnification**: Numeric value of the magnification used to acquire the image.
15. **microscopy.fov**: Field of view, well site, or microscope position in the well when the channel was captured.
16. **geometry.width**: Channel width in pixels.
17. **geometry.height**: Channel height in pixels.
18. **geometry.depth**: Total number of z-planes this channel belongs to, if the study is a 3D imaging assay.
19. **geometry.channels**: Total number of sibling channels in the same image.
20. **geometry.z_slice**: Number of the z-plane for this channel. It is a numerical value.
21. **geometry.timepoint**: Number of the frame in the timelapse sequence, if applicable.
22. **storage.path**: File path of the PNG file in the dataset containing this channel

A.5 Metadata quality and handling inconsistencies

The construction of `CHAMMI-75` involved integrating 75 heterogeneous studies, many of which lacked standardized or complete metadata, reflecting a general deficiency in data sharing practices across biology. Our approach to handling missing, inconsistent, and ambiguous data was rigorous yet pragmatic, acknowledging that perfect retrospective standardization is often impossible.

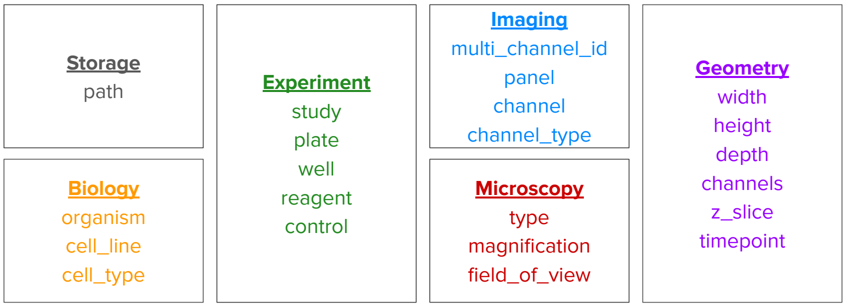

Figure A9: Visualization of metadata fields in six groups and 22 fields.

Handling missing data. The vast majority of studies provided partial metadata. For fields where information was unequivocally absent (e.g., biology.cell_type or microscopy.fov), the entry was explicitly and consistently annotated with the string ”unknown”. This approach avoids using null values or empty strings, ensuring consistency for subsequent programmatic access and filtering.

Resolving ambiguity and inconsistency. In cases where metadata was ambiguous (e.g., multiple spellings for a cell line, or an overly verbose stain identity), we employed a multi-step resolution pipeline: (1) Cross-reference: values were validated against other metadata columns (e.g., cross-checking organism and cell line). (2) External validation: we performed targeted web searches and reviewed the associated scientific publications to infer the most likely accurate value. (3) LLM-assisted parsing: As noted in Appendix A.3, we used LLMs to systematically extract and organize certain information, providing a rapid, initial pass at resolving naming variants and extracting structured data from free-form text descriptions. (4) Manual curation and normalization: to minimize inconsistencies, all resulting values were manually reviewed, low-cased, and mapped to a simplified vocabulary or ontology where possible (e.g., different fluorescence channels like ’DAPI’, ’Hoechst 33342’, and ’Nuclear stain’ were often mapped under the canonical channel_type of ’nucleus’).

Last resource. If, after all these steps, the interpretation remained uncertain (e.g., a stain was ambiguously described and the original publication offered no clarity), we defaulted to preserving the original value or, more conservatively, labeling the entry as ”unknown”.

The resulting metadata table, while significantly cleaned, remains inherently noisy. We view this noise and high sparsity (Figure 4b) not as a limitation, but as a defining feature of the resource. Unlike highly standardized datasets produced synchronously by a single consortium, `CHAMMI-75` attempted to align data that were never intended for cross-study integration. This noisy complexity presents the real-world challenge foundation models for bioimaging must solve –to learn representations that are robust despite inconsistent. Future efforts should focus on promoting standardized metadata acquisition for new studies (Schmied et al., 2024), as retrospectively fixing metadata is computationally infeasible and prone to subjective error. Furthermore, our dataset provides a compelling target for future research into semi-automated, multi-modal systems capable of resolving these remaining metadata inconsistencies.

A.6 Data Sources

The following are the official data sources or hosting platforms where we obtained microscopy images to curate the `CHAMMI-75` dataset in alphabetical order: Allen Institute (Viana et al., 2023), AMSActa (of Bologna, 2025), BBBC (Ljosa et al., 2012), BioImage Archive (Hartley et al., 2022), BioStudies, Cell Painting Gallery (Weisbart et al., 2024), Edmond (Society, 2025), EMPIAR (Iudin et al., 2023), Figshare (Singh, 2011), GitHub (Kaggle, 2025), HPA (Thul et al., 2017), IDR (Williams et al., 2017), Mendeley Data (Elsevier, 2025), OSF (OSF, 2025), Recursion (Recursion, 2025), University of Reading Research Data Archive (of Reading, 2025), Zenodo (CERN & OpenAIRE, 2013). Each of the 75 datasets are listed in Table A6 with their corresponding licenses, number of channels per image, and the number of multi-channel images sampled from the original dataset.

Table A6: Image Dataset Information

ID	Dataset	License	Channels	Images
CellPHIE	CellPHIE (Broad Institute) (Kang et al., 2025)	CC BY-NC 4.0	14	57,021
hpa0018	HPAv18 (HPA) (Thul et al., 2017)	CC BY-SA 4.0	4	113,545
hpa0023	HPAv23 (HPA) (Thul et al., 2017)	CC BY-SA 4.0	4	249,999
idr0001	IDR0001 (IDR) (Graml et al., 2014)	CC BY 4.0	2	112,476
idr0002	IDR0002 (IDR) (Hériché et al., 2014)	CC BY 4.0	2	27,092
idr0003	IDR0003 (IDR) (Breker et al., 2013)	CC BY-NC-SA 3.0	3	43,072
idr0005	IDR0005 (IDR) (Toret et al., 2014)	CC BY-NC-SA 3.0	1	34,698
idr0006	IDR0006 (IDR) (Fong et al., 2013)	CC BY-NC-SA 3.0	2	125,508
idr0007	IDR0007 (IDR) (Srikumar et al., 2013)	CC BY-NC-SA 3.0	2	3,213
idr0008	IDR0008 (IDR) (Rohn et al., 2011)	CC BY-NC-SA 3.0	4	23,159
idr0009	IDR0009 (IDR) (Simpson et al., 2012)	CC BY 4.0	3	86,116
idr0010	IDR0010 (IDR) (Doil et al., 2009)	CC BY 4.0	2	44,761
idr0011	IDR0011 (IDR) (Ledesma-Fernández & Thorpe, 2015)	CC BY 4.0	3	17,893
idr0012	IDR0012 (IDR) (Fuchs et al., 2010)	CC BY-NC-ND 4.0	3	22,182
idr0013	IDR0013 (IDR) (Neumann et al., 2010)	CC0 1.0	1	208,474
idr0017	IDR0017 (IDR) (Breinig et al., 2015)	CC BY-NC-ND 4.0	2	65,048
idr0022	IDR0022 (IDR) (Koedoot et al., 2019)	CC BY 4.0	1	54,690
idr0025	IDR0025 (IDR) (Stadler et al., 2012)	CC BY-SA 3.0	4	564
idr0028	IDR0028 (IDR) (Pascual-Vargas et al., 2017)	CC BY 4.0	4	33,707
idr0030	IDR0030 (IDR) (Sero & Bakal, 2017)	CC BY 4.0	4	38,017
idr0033	IDR0033 (IDR) (Rohban et al., 2017)	CC BY 4.0	5	16,024
idr0035	IDR0035 (IDR) (Ljosa et al., 2013)	CC BY 4.0	3	11,403
idr0037	IDR0037 (IDR) (Vigilante et al., 2019)	CC BY 4.0	5	17,617
idr0056	IDR0056 (IDR) (Stojic et al., 2020)	CC BY 4.0	5	50,177
idr0069	IDR0069 (IDR) (Caldera et al., 2019)	CC BY-NC 4.0	3	82,812
idr0072	IDR0072 (IDR) (Schormann et al., 2020)	CC BY 4.0	2	68,642
idr0080	IDR0080 (IDR) (Way et al., 2021)	CC0 1.0	5	11,425
idr0081	IDR0081 (IDR) (Georgi et al., 2020)	CC BY 4.0	2	10,040
idr0086	IDR0086 (IDR) (Miron et al., 2020)	CC BY 4.0	6	15,283
idr0088	IDR0088 (IDR) (Cox et al., 2020)	CC BY-NC 4.0	3	151,021
idr0089	IDR0089 (IDR) (Fischl et al., 2020)	CC BY 4.0	3	8,077
idr0093	IDR0093 (IDR) (Müller et al., 2021)	CC BY 4.0	5	44,858
idr0094	IDR0094 (IDR) (Ellinger et al., 2021)	CC0 1.0	1	65,828
idr0115	IDR0115 (IDR) (Otsuka et al., 2023)	CC BY 4.0	2	13,273
idr0120	IDR0120 (IDR) (German et al., 2021)	CC BY 4.0	5	33,390
idr0123	IDR0123 (IDR) (Mota et al., 2022)	CC BY 4.0	7	3,157
idr0128	IDR0128 (IDR) (Olszewski et al., 2022)	CC BY 4.0	2	9,539
idr0129	IDR0129 (IDR) (Olszewski et al., 2022)	CC BY 4.0	2	10,441
idr0130	IDR0130 (IDR) (Olszewski et al., 2022)	CC BY 4.0	2	3,785
idr0133	IDR0133 (IDR) (Dahlin et al., 2023)	CC BY 4.0	5	23,149
idr0140	IDR0140 (IDR) (Ho et al., 2022)	CC BY 4.0	2	16,721
idr0145	IDR0145 (IDR) (Ho et al., 2023)	CC BY 4.0	2	16,338
jump0001	cpg0016-jump (Cell Painting Gallery) (Chandrasekaran et al., 2023b)	CC0 1.0	5	146,741
nidr0001	ALFI (Figshare) (Antonelli et al., 2023)	CC BY 4.0	1	2,146
nidr0002	Stomata (Mendeley Data) (Dey et al., 2023)	CC BY 4.0	3	1,004
nidr0003	S-BIAD531 and S-BIAD840 (BioImage Archive) (Jones et al., 2024)	CC0 1.0	1	15,056
nidr0004	White blood cells (Figshare) (Bodzas et al., 2023)	CC BY 4.0	3	14,565
nidr0005	BriFiSeg (Zenodo) (Mathieu et al., 2022)	CC BY 4.0	1	1,029
nidr0006	VirtualStaining (Figshare) (Trizna et al., 2023)	CC BY 4.0	4	252
nidr0007	S-BIAD300 (BioImage Archive) (Yakimovich & Galimov, 2021)	CC0	1	31,558
nidr0008	BBBC030 (BBBC) (Koos et al., 2016)	CC BY 4.0	1	60
nidr0009	Parasites (Mendeley Data) (Zhang et al., 2022)	CC BY 4.0	3	297
nidr0010	DICimages (University of Reading Research Data Archive) (Kempster et al., 2022)	CC BY 4.0	1	132
nidr0011	PerceptiLabs/bacteria (GitHub)	CC0 1.0	1	366
nidr0012	DeepBacs1 (Zenodo) (Spahn et al., 2022)	CC BY 4.0	1	99
nidr0013	DeepBacs2 (Zenodo) (Spahn et al., 2022)	CC BY 4.0	1	60
nidr0014	DeepBacs3 (Zenodo) (Spahn et al., 2022)	CC BY 4.0	1	34
nidr0015	EVICAN (Edmond) (Schwendy et al., 2020)	CC BY 4.0	1	4,361
nidr0016	Fluorescent Neuronal Cells v2 (AMSActa) (Clissa et al., 2024)	CC BY 4.0	2	1,809
nidr0017	LIVECell (Figshare) (Edlund et al., 2021)	CC BY 4.0	1	5,165
nidr0018	Omnipose (OSF) (Cutler et al., 2022)	CC BY-NC 3.0	1	791
nidr0019	BBBC042 (BBBC) (Suleymanova et al., 2018)	CC BY 4.0	1	1,054
nidr0020	VISEM-Tracking (Zenodo) (Thambawita et al., 2023)	CC BY 4.0	3	13,608
nidr0021	WBC1 (Mendeley Data) (Zheng et al., 2018)	CC BY-NC 3.0	3	300
nidr0022	WBC2 (Mendeley Data) (Zheng et al., 2018)	CC BY-NC 3.0	3	100
nidr0023	S-BSST265 (BioImage Archive) (Kromp et al., 2020)	CC0 1.0	1	79
nidr0024	CEM500K (EMPIAR) (Conrad & Narayan, 2021)	CC0 1.0	1	264,187
nidr0025	S-EPMC8322260 (BioStudies) (Khoshkenar et al., 2021)	CC BY 4.0	2	81
nidr0027	Microscopic peripheral blood (Mendeley Data) (Acevedo et al., 2020)	CC BY 4.0	3	15,710

Continued on next page

Continued from previous page

ID	Dataset	License	Channels	Images
nidr0028	Three fold annotated potato dataset (Figshare) (Biswas & Barma, 2020)	CC BY 4.0	3	14,269
nidr0029	RxRx19a (Recursion) (Heiser et al., 2020)	CC BY 4.0	5	60,594
nidr0030	RxRx19b (Recursion) (Cuccarese et al., 2020)	CC BY 4.0	6	34,787
nidr0031	RxRx1 (Recursion) (Sypetkowski et al., 2023)	Recursion Custom Commercial License	6	26,328
nidr0032	RxRx2 (Recursion) (Cuccarese et al., 2020)	CC BY-NC-SA 4.0	6	30,744
wtc0001	WTC-11 (Allen Institute) (Viana et al., 2023)	Allen Institute Terms of Use	4	117,882
			Total	**2,849,483**

A.7 Comparison to other datasets

These datasets were chosen for comparision as our dataset is not a biological study but rather an AI-ready dataset to investigate single-cellular morphology foundation models. Our data set is not a reference set for interactive querying because it contains diverse samples from heterogeneous studies in a way optimized for machine learning, not for biological discoveries. We have compared our data set against similar imaging data sets that are ready for machine ingestion and have been used in relevant work to build foundation models in cellular morphology. All the numbers used in Figure 2 are reported in the table A7.

Table A7: Overview of Multi-Channel Image Datasets.

Name	**Images**	**Src**	**Ch.**	**Org.**	**Access**	**Cite**
CHAMMI-75	2,849,483	75	25	Multi-channel	Public	**Ours**
CHAMMI	220,284	3	8	Multi-channel	Public	(Chen et al., 2023)
RxRx	4,168,973	6	6	Fixed-channel	Public	(Recursion, 2025)
Jump-CP	8,109,884	12	5	Fixed-channel	Public	(Chandrasekaran et al., 2023a)
HPAv23	1,138,378	1	4	Fixed-channel	Public	(Gupta et al., 2024)
IDRCell100k	104,093	79	10	Multi-channel	Public	(Bourriez et al., 2024)
Phenoprints-16M	16,000,000	1	6	Fixed-channel	Private	(Kenyon-Dean et al., 2024)
CytoImageNet	890,737	40	12	Mixed-channel	Public	(Hua et al., 2021)
Microsnoop	2,230,000	7	3	Mixed-channel	Public	(Xun et al., 2024)

Src refers to Source. Org. refers to the type of organization of the dataset and whether it was multi-channel, fixed-channel or mixed-channel. Multi-channel means that it has images with images having varied number of channelled images, Fixed-channel means that the images only have one configuration of channels. Mixed channel mean if they originally had images with varied number of channels but the channel order and information was not preserved properly.

A.8 Cell segmentation and cellular scales

We used the Cyto3 model in Cellpose (Pachitariu & Stringer, 2022) to segment all the different 75 studies in our dataset to obtain centroid coordinates of all these different microscopy images at the single-cell level. Our goal was to segment the nucleus of the cells as that was the most consistent channel type present in all the studies. We manually configured Cellpose parameters such as size, and channels used for segmentation to improve segmentation quality. We have found 300 million cells in the small version of our dataset and almost 1.8 billion cells (1,791,151,533 cells) in the large version of our dataset. Figure A10 provides a quantitative background about the segmentation results.

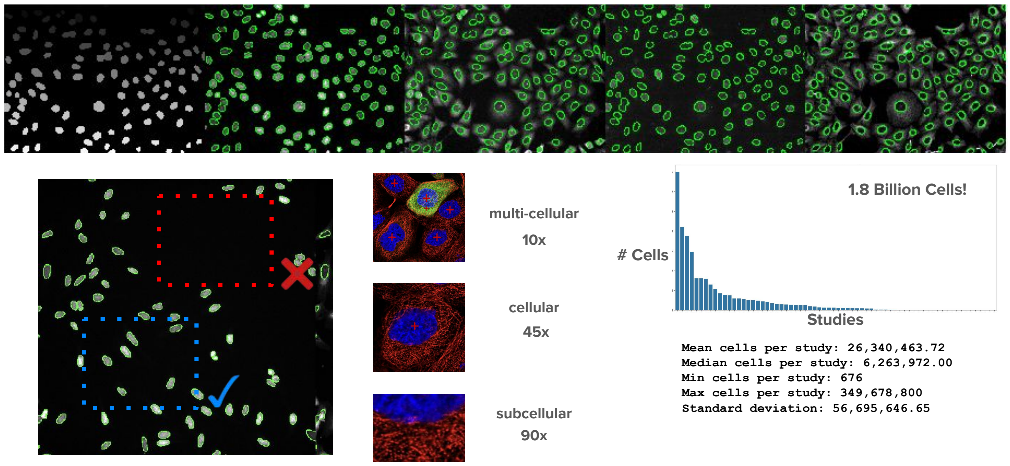

```
Mean cells per study: 26,340,463.72
Median cells per study: 6,263,972.00
Min cells per study: 676
Max cells per study: 349,678,800
Standard deviation: 56,695,646.65
```

Figure A10: Segmentation pipeline examples.

It takes 7 days on 8 NVIDIA L40s GPUs to segment all multi-channel images in `CHAMMI-75`. Once all images were segmented, we found that the area taken by the segmented nucleus on microscopy images is 19.12%, which means that 80.88% of the nucleus image is empty. To counteract this issue, we used our single cell coordinates to do guided crops during our model training. We also annotated average cell sizes in all 75 studies, which helped us observe the cellular structures at different scale levels similar to how magnification levels are discrete in microscopy.

Cell scales. We manually determined crop sizes that contain subcellular, cellular, or multi-cellular views and created study-level annotations for the 75 sources. The resolution of some studies may only allow access to one or two of the three scales. These annotations are helpful to crop and resize images in a predictable way.

We have developed cellular scale annotations at the multi-cellular scale and the cellular scale. These annotations were obtained manually for all the different cellular scale levels. We set the cell centroid for an image in the middle and crop the scale accordingly.

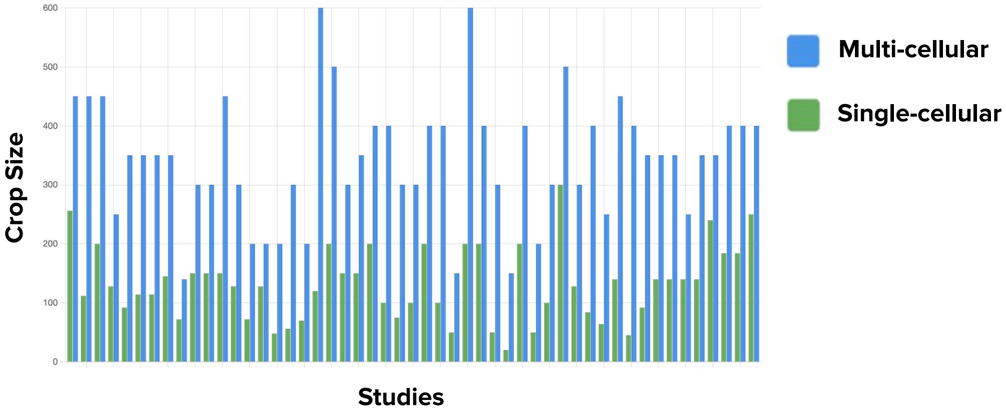

Figure A11: Histogram of cellular-level annotations

Data loader. In combination, the single-cell coordinates and the scale annotations are useful information to design data loaders that generate fixed-size crops with the desired properties. We implemented a data loader that samples image content hierarchically in the following way: 1) randomly select a multi-channel image, 2) randomly select a single cell from the coordinates table, 3) randomly select an available scale size, 4) crop a region around the cell location with the selected scale size and then resize to a standard model input size, 5) finally, apply any additional transformations or augmentations. This design can be modified or expanded to explore other multi-scale learning approaches.

Content annotations. The heterogeneous images in `CHAMMI-75` have different sizes, magnifications, and resolutions, which departs from the standard practice of assuming a fixed configuration for all images. This means that a random crop from an image in `CHAMMI-75` may contain multiple cells, a single cell, or a subcellular structure. This lack of alignment in scales can be a challenge for representation learning algorithms. We created study-level, scale annotations for the 75 sources to determine the views available in an image (subcellular, cellular, multi-cellular). We implemented a content-aware, hierarchical data loader for training that leverages cell coordinates and scale annotations.

A.9 Evaluation Datasets and Benchmarks

IDR-0017. This benchmark aims to reproduce the findings of the IDR017 study: A Chemical-Genetic Interaction Map of Small Molecules (Breinig et al., 2015). The study evaluates gene-compound interactions by treating 1,280 compounds on 12 isogenic cell-lines using high-throughput imaging techniques. It extracts image-based features at the single-cell level to quantify phenotypic changes under a combinatorial study that aims to understand drug mechanisms and target effects.

The biological experiment behind the images aims to determine whether a cell-line (with a mutated gene) responds to specific chemical treatments. A control experiment consists of a cell-line without chemical treatment, and then other treatments are applied to evaluate if there is any difference between using the treatments or not. When a difference between the control experiment and the effect of a treatment is large enough, the chemical treatment is labeled as a hit. In this study, there are a total of 1,280 × 12 = 15,360 combinatorial experiments which identified 193 hits. To identify hits, the original study used 20 manually engineered features at the single-cell level, including cell size, actin intensity, nucleus intensity, cell shape and nuclear shape.

The dataset consists of approximately 150k two-channel images across 96 384-multi-well plates. The two channels are: a nucleus marker and a cytoskeleton marker, and 4 fields of view are acquired per well at 10X magnification in 2048x2048 pixel images. Each plate contains controls followed by treated cells, and the study is performed across 2 replicates on 2 different set of plates. The original dataset was obtained from IDR (Williams et al., 2017), and we pre-processed the images to facilitate standardized analysis as follows: 1) Performed cell segmentation using cellpose model using nucleus and cytoskeleton channel. 2) sampled 512 x 512 patch from every image based on cell density using segmentation maps to reduce the number of cells to analyze. This method help us to reduce the average cell count from 2300 cells to 200 cells per image. 3) Patches of 100 x 100 are sampled across single cells for feature extraction.

To transform the original analysis into an evaluation benchmark, we start computing features using trained models to approximate the representation of the phenotypic changes at the single-cell level. To identify hits, we use the model embeddings from images of the same treatment to calculate the effect size with respect to control cells. The single-cell embeddings are aggregated by taking the mean per image and two Eucledian distance matrices are constructed: one for the treatment vs control images, and another one for the control vs control images. The effect size of a compound is estimated using the Wasserstein distance between the distance matrices of control and treatment image embeddings. To avoid batch effects, we aggregate both replicates for each compound using PCA whitening normalization. The compounds for each cell line are ranked on the basis of the effect score. We use Recall@50, Recall@100, and AUROC as metrics to measure how well a model ranks high-interaction compounds above low-interaction compounds.

HPAv23 at 256x256. The HPAv23 subcellular benchmark was released with the SubCell model(Gupta et al., 2024). The dataset was originally curated in the 23rd version of the Human Protein Atlas Project (Thul et al., 2017). The authors of (Gupta et al., 2024) made crops of the images to allow machine ingestion, and develop a benchmark for the same. This benchmark provides a granular detail needed to test whether current models can identify meaningful subcellular differences in cellular organization.

The dataset is a collection of immunofluorescence images encoding the expression and spatiotemporal distribution of 13,141 genes in 37 cell lines. The images were stained with DAPI, a fluorescent dye that labels the nucleus, and antibodies labeling endoplasmic reticulum (ER), microtubules (MT) and protein of interest (protein). The images were cropped from FOV images to single cell images that contained 1,138,378 cells. The data set was split by the original authors based on antibodies with a ratio of 7: 1: 2 into training, validation, and test sets, respectively. (Gupta et al., 2024) used a multilabel stratification strategy to ensure a similar multilabel distribution between the sets.

The protein localization task we have adapted paper is a supervised learning task using a multi-layer perceptron (MLP) on the features obtained from a frozen backbone of all the models. The MLP classifier uses the same three-layer classifier architecture as (Kraus et al., 2024) and focal loss (Cho et al., 2022) to address class imbalance in the dataset. The classifiers were trained on features extracted from the whole HPAv23 set including the pre-training set, and the rest of the images. Unlike the original authors, we downsampled all images from 1024×1024 to 256×256 to accelerate the benchmark, reduce its time complexity, and decrease storage requirements. We are re-releasing this reformatted set with our dataset to enable easy usage of this benchmark. The task has two sets of classifier: the first set us comprised of 19 categories specified in Kaggle challenge, and the second set has a broader range of 31 categories. We have reported the micro and macro average precision (AP) as the classification metrics and used multilabel ranking average error and coaverage error to evaluate multilabel performance on the test sets just like the original authors. The challenge category results are reported in the main text in 1, 2 and D15. The results of the unique category are reported in D16

JUMP-CP1 Compounds. In this benchmark, the quality of the replicate level and consensus treatment profiles is evaluated in a subset of the JUMP-CP1 dataset (Chandrasekaran et al., 2023b) for the compounds that were originally curated with Broad Institute's Drug Repurposing Hub. Cell Painting assay (Bray et al., 2016) was used, where six fluorescent dyes highlight eight cellular compartments that are imaged in five channels at 20X magnification.

From a biological perspective, the aim is to capture meaningful differences between populations of cells with respect to the perturbation and the target of this perturbation. Those differences between cell states might be subtle and hard to detect for certain types of perturbations even against negative control (unperturbed) cells. The quality of the replicate level profiles is defined by the closeness of a given perturbation replicates against a set of negative control replicates. The quality of treatment-level profiles is evaluated by the closeness of profiles with the same biological label (in this case, gene target) against other perturbations. Both metrics are introduced and implemented in *copairs* benchmarking suite (Kalinin et al., 2025).

Originally, JUMP-CP1 includes many biological and experimental conditions: two cell lines (A549 and U2OS), three perturbation types (chemical compounds, gene open reading frame (ORF) overexpression and CRISPR-Cas9 knockouts) captured at two time points. For this benchmark, we used only the data from the U2OS cell line and chemical compound perturbations at both time points, eventually having a similar set of seven 384-well plates that matches the one used in the evaluation of SubCell (Gupta et al., 2024). The images from the evaluation plates are not used in the pre-training set. Original 16-bit TIFF images (24,192 fields of view – 120,960 single-channel images in total) were normalized and compressed to 8-bit PNG images with DeepProfiler (Moshkov et al., 2024) *prepare* option and then single-cell crops were exported with *export-sc* option, using the cell locations provided with the original CellProfiler features, resulting in 2M unmasked cell-centered crops (”cells in context”).

In this benchmark, we start by computing features for single-cell crops that are saved at size 160x160 and that are further cropped to size 128x128. The final 128x128 input images are resized to accommodate to the expected input size of the particular model at use. Single-cell feature vectors are then aggregated using mean aggregation to the well-level (replicate) profiles. Well-level profiles are then batch corrected with ZCA-whitening from pyCytominer package (Serrano et al., 2025) relative to negative controls with $epsilon = 0.001$. This data is then used in the benchmark: *copairs* returns mAP and p-value for each perturbation (phenotypic activity) and target (phenotypic consistency). We report the mean mAP for phenotypic activity as *JUMP-CP1*. For treatments that did not pass the 0.05 p-value threshold, we assume $mAP = 0$. We report mean mAP for phenotypic consistency as *JUMP-CP2*. Similarly, for targets that did not pass 0.05 p-value threshold, we assign $mAP = 0$. As phenotypic consistency is calculated only for treatments that passed p-value threshold for phenotypic activity, some targets might not be represented in this step of benchmark. We also assign $mAP = 0$ to such missing targets.

CellPHIE. This study used iPSC-derived neurons to investigate genetic and morphological markers of Huntington's Disease using the latest generation of pooled genetic perturbations at the single-cell level with a multiplexed optical screen. The dataset contains a total of 57,021 images out of which 45,782 training images and 11,239 testing images. The original images from the dataset were filtered, and we kept images from DS28 time sample, and we removed two genes from the original set which were DGKE and GAS7 genes. Single-cell images segmented, cropped and masked at 64x64 pixels. The imaging panel consists of 5 Cell Painting channels and 9 protein markers obtained with immunofluorescence, for a total of 14 imaging channels. The 14 channels in the images are in the following order: DNA, NeuN, pRPS6, RANGAP1, NFKB, TOM20, LAMP1, TDP43, G3BP1, GM130, Golgin97, SYTO, ER, AGP. Channels 2 to 10 are protein channels.

Each single cell was perturbed with one of 19 genes, which was identified with optical barcoding. From the 19 perturbations, one is a non-targetting control used as a reference to determine the effect of other preturbations. The task in this benchmark is to classify single cells in a binary classification setting: non-targeting vs perturbed gene. The dataset has a training / validation split to evaluate performance using a linear probe. Note that none of the images in CellPHIE were included in the `CHAMMI-75` training set, representing a fully held-out set with novel channel combinations and the largest number of channels in the benchmark.

RBC-MC. This benchmark is based on bright-field microscopy imaging of red blood cells (RBCs) from Doan et al. (Doan et al., 2020) containing one channel. The dataset comprises RBC samples collected from two geographically distinct blood banks located in Switzerland and Canada. Following the experimental protocol, we train a logistic regression classifier on one dataset and evaluate its performance on the other to assess cross-dataset generalization. The benchmark consists of 76,577 images from the Swiss dataset and 46,695 images from the Canadian dataset, with all images uniformly sized at 48×48 pixels. RBC morphology is categorized into seven distinct classes: Smooth Disc, Crenated Disc, Crenated Discoid, Crenated Spheroid, Crenated Sphere, Smooth Sphere, and Side View. Images originally labeled as ”Undecided” by expert annotators, indicating uncertainty in morphological classification, were excluded from the benchmark to ensure label quality.

B Factors Affecting Representation Learning

B.1 Motivation

Understanding the drivers of effective representation learning in microscopic imaging is crucial for developing robust computer vision models in this domain. We systematically investigated how various factors influence the quality of learned representations, focusing on cell line diversity, imaging modality variety, channel configurations, and data similarity to the target domain. A key finding emerged during our investigation: all factors of variation are confounded with each other. When ablating one variable, we consistently observed substantial changes in other variables, indicating complex interdependencies. We examined four primary factors:

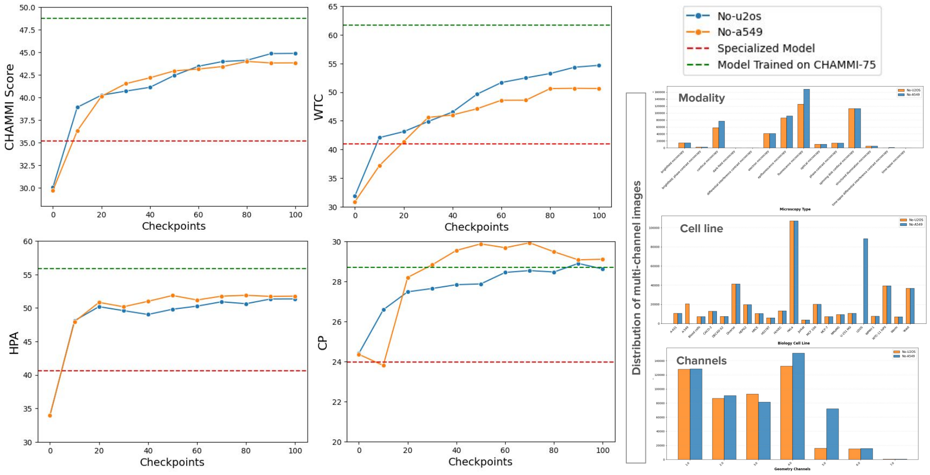

Figure B12: Showcasing Cell Line Ablations of U2OS and A-459 compared to the Specialized Models and model trained on `CHAMMI-75`

- Cell Line Ablation
- Modality Ablation
- Channel Number Variation
- Data Similarity To Target Domain

B.2 Cell Line Ablation

We conducted ablation studies comparing the removal of the dominant cell line (U2OS) versus a less prevalent line (A459) from our training data. Although our data scaling analysis (Figure 7) confirmed that larger datasets generally improve performance, ablating U2OS—despite reducing total training data—yielded a 2 percentage point improvement over ablating A459.

This counterintuitive result demonstrates that greater cell line diversity provides more value than simply maximizing data volume from a single dominant source. The findings suggest that representation learning benefits more from exposure to varied biological contexts, even when this comes at the cost of fewer total samples per cell line (Figure B12).

B.3 Modality Ablation

To isolate the effect of modality diversity, we trained two separate DINO Bag-of-Channels (BoC) models. The first model was trained exclusively on two microscopy modalities—fluorescence and epifluorescence—comprising 790,000 images. The second model incorporated the remaining 13 modalities, totaling 880,000 images.

Despite having only 11 percentage more data, the 13-modality model substantially outperformed the 2-modality model, achieving approximately 5 percentage points higher performance on the CHAMMI benchmark. This result contradicts simple data scaling predictions, which would favor the larger dataset. Instead, our findings underscore that modality diversity is a more critical factor than raw data volume.

These results align with previous work by (Arevalo et al., 2024), who identified microscopy type as the dominant confounding factor in batch correction studies. This convergent evidence suggests that exposure to diverse imaging modalities drives the learning of robust, generalizable representations that transfer effectively across different imaging contexts (Figure B13).

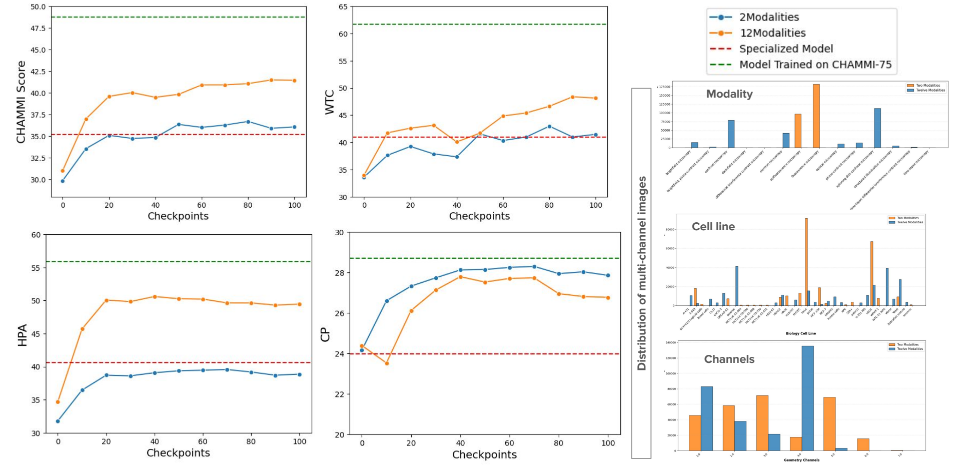

Figure B13: Showcasing Modality Ablations of having 2 modalities versus 13 modalities compared to the Specialized Models and model trained on `CHAMMI-75`

B.4 Channel Number Ablation

We investigated whether the number of imaging channels influences representation quality by training DINO BoC models on study subsets with varying channel counts (2, 3, 4, and 5 channels). Since incorporating studies with more channels inherently increases total data volume, naive comparisons might conflate channel count effects with data scaling effects.

To control for this confound, we fixed all models to 500,000 training iterations, ensuring computational budget parity. Under these controlled conditions, we observed no substantial performance variations attributable to channel count (Figure B14). This null result is expected given that the BoC architecture does not explicitly model inter-channel interactions, treating each channel independently.

Whether modeling inter-channel dependencies could yield improvements over BoC approaches remains an open research question. While several methods have explored this direction—including (Bao et al., 2023), (Bourriez et al., 2024), and (De Lorenci et al., 2025) approaches—none have yet demonstrated clear superiority over BoC methods. Our dataset, with its diverse channel configurations across studies, provides a valuable resource for future investigations into this question.

B.5 Data Similarity To Target Domain

We systematically analyzed how training data similarity to the target evaluation set affects representation learning. Our methodology involved extracting features from 1,000 single cells per study and channel type, totaling 75,000 cells across our dataset. We performed identical feature extraction on the CHAMMI-HPA test set using our best-performing DINO BoC model.

To quantify similarity between training and test data, we computed average feature vectors for each study and channel combination (processing each channel independently). Using Euclidean distance between these average vectors, we identified which training studies most closely resembled the test set. Based on this similarity metric, we selected two subsets: the top 20 percentage most similar studies and the bottom 20 percentage most dissimilar studies. We then trained separate self-supervised DINO BoC models on each subset.

The results revealed a nuanced relationship between data similarity and model performance. While the model trained on similar data showed improved performance specifically on the HPA benchmark, suggesting some benefit from domain alignment, its overall performance across the broader evaluation suite was inferior to the model trained on dissimilar data (Figure B15). This counterintuitive finding indicates that diverse, dissimilar training data

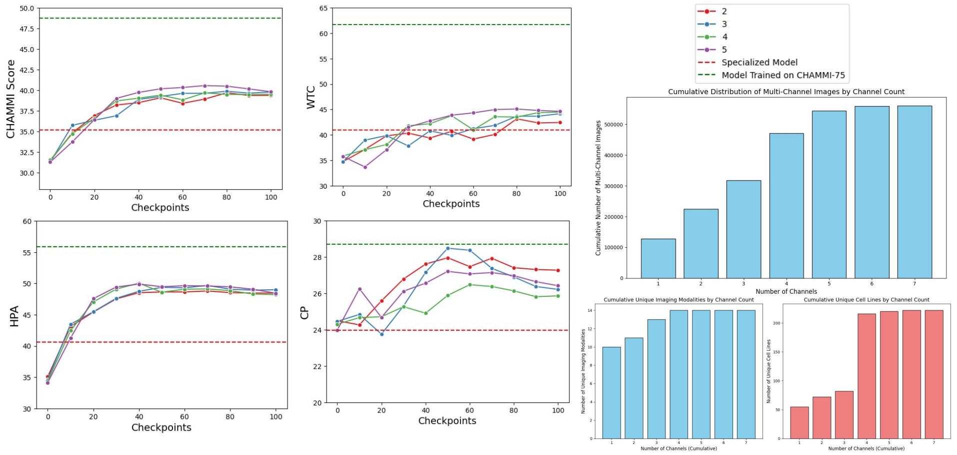

Figure B14: Showcasing Channel number variations with fixed compute of 500k compared to the Specialized Models and model trained on `CHAMMI-75`

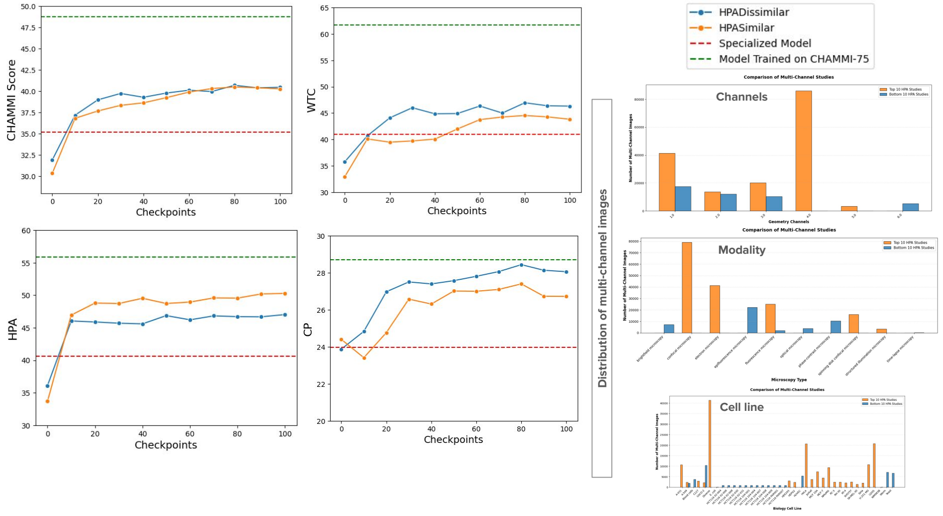

Figure B15: Showcasing Similar Data vs Dissimilar Data compared to the Specialized Models and model trained on `CHAMMI-75`

promotes learning of more generalizable representations, even if it means sacrificing some degree of specialization to the target domain.

This result reinforces our broader finding that diversity in training data is a key driver of robust representation learning. Models trained on dissimilar data are exposed to a wider range of biological and imaging contexts, which appears to facilitate the learning of features that transfer more effectively across diverse microscopy tasks. While domain-specific fine-tuning on similar data may benefit specialized applications, diverse pre-training appears essential for building generally applicable microscopy foundation models.

C Scalability Analysis Details

To train multi-channel ViTs, prior work has explored supervised (e.g., Channel-ViT (Bao et al., 2023)), self-supervised (e.g., CA-MAE (Kraus et al., 2024), ChADa-ViT (Bourriez et al., 2024)), or hybrid multi-task objectives (e.g., ChA-MAEViT (Pham et al., 2025)).

CHAMMI-75 is a pre-training dataset primarily useful for self-supervised, potentially useful for weakly supervised, and not useful for fully supervised learning. We explore SSL algorithms to train a multi-channel model using CHAMMI-75 with the goal of learning cellular morphology representations for solving diverse downstream tasks. Here, we evaluate well-established, representative algorithms from three major families of self-supervised learning methods for images: (1) SimCLR (contrastive) (Chen et al., 2020), (2) Masked Autoencoders (reconstructive) (He et al., 2022), and (3) DINO (self-distillation) (Caron et al., 2021).

To evaluate CHAMMI-75 as a pre-training resource, we compare performance by training with varying configurations. First, we evaluate the performance of models trained with an increasing amount of multi-channel images, which we call "*dataset scaling*" evaluation. Performance is evaluated on the CHAMMI benchmark (Chen et al., 2023), which has six out-of-distribution, phenotype matching tasks. We train models specialized on a fixed channel configuration as a baseline (1ds, 33K images per dataset; 3,4,&5 channels), and then combine sets to increase channel types and source variation, starting with the 3 CHAMMI subsets (3ds, 100K images, 8 channels), 10 datasets (10ds, 178K images, 14 channels), and a sample of the images in the 74 pre-training datasets from CHAMMI-75 (74ds-small, 560K images, 25 channels). We leave the full CHAMMI-75-set (74ds-large, 2.8M images, 25 channels) out of the scaling evaluation; we only used it for the main benchmarking experiment following the best configuration in our analysis. We also conduct a "*model scaling*" evaluation, where we keep the dataset size fixed (74ds-small) and grow model parameters.

Experimental and implementation details. We train two types of ViT models: bag of channels (BoC) and multi-channel attention (MCA). The input size for all models is 224x224 pixels, and the number of channels is either one (BoC) or variable (MCA). Models are trained with one of the three selected SSL algorithms (SimCLR, MAE, DINO), and we keep hyper-parameters as constant across experiments as possible and apply relevant tweaks to avoid optimization divergence or collapse. After a model is trained with SSL, we keep the weights frozen and extract features in the three test sets of the CHAMMI benchmark without any finetuning. We use the PyTorch framework and we run experiments using multi-GPU training with 4 to 8 GPUs typically in a single node. All experiments were conducted in academic compute clusters (Appendix G.2).

Results. Consistent with previous studies, we find that models trained with SSL benefit from having access to more data (He et al., 2022; Oquab et al., 2023; Siméoni et al., 2025). We compare performance against the top-line of specialized models trained for each of the three subsets with fixed channels and with full supervision. This serves as an upper-bound reference to assess performance of models trained with SSL. The results are presented in Figure 8, and confirm that as we increase the dataset size and the model size, SSL models approach the performance of specialized, supervised models. This indicates that a single, multi-channel model trained at scale without supervision can be highly competitive in various downstream tasks.

We observe that the top factor that determines performance is the multi-channel strategy (BoC or MCA), followed by type of SSL algorithm, and model size. BoC models yield better performance than MCA models in the SSL regime, indicating that cross-channel correlations remain difficult to learn without supervision. We find BoC models easier to scale than MCA models because the latter has longer sequences that have high memory and compute requirements. MCA models required between 3X and 5X more GPU hours than BoC to complete a training session with the same amount of data (Figure G21). In addition, SSL algorithms perform comparably within multi-channel strategies (BoC or MCA), with DINO consistently outperforming the others.

Based on these results, we trained a BoC ViT-small model with the DINO algorithm using the full CHAMMI-75 dataset, which has 5X more data than the 74ds small set, and required 2,352 GPU hours to complete (7 days with 2x7-GPU servers). The result of this experiment followed the performance improvement trend obtaining a 9.8% relative improvement over the best result in the dataset scaling evaluation. The model scaling results suggest that additional performance gains could be obtained with larger ViT architectures, which we did not explore in this work.

D Benchmark results

We will take a look at a larger resolution of numbers for all the benchmarks with more related results for better analysis.

D.1 CHAMMI

CHAMMI is the benchmark for multi-channel microscopy imaging presented in (Chen et al., 2023). Here, we show all the values for CHAMMI showcased for dataset scaling laws in D8. We show sub-scores for WTC, HPA, and CP in D9, D10, and D11 respectively.

Table D8: Summary of IID Mean, CHAMMI Scores for WTC, HPA, and CP sets

Model	**IID Mean**	**CHAMMI Score**	**WTC**	**HPA**	**CP**
BoC (ViT Small) ours	84.26	48.75	61.72	55.84	28.71
OpenPhenom (ViT Small)	75.55	38.23	42.80	43.15	28.74
DINOv2 (ViT Small)	73.95	37.93	46.27	39.66	27.87
IDRCell (ViT Small)	68.55	37.38	45.29	40.40	26.44

Table D9: WTC Dataset Benchmark Scores

Model	**Task 1**	**Task 2**
BoC (ViT Small) ours	72.56	61.72
OpenPhenom (ViT Small)	59.72	42.80
DINOv2 (ViT Small)	63.56	46.27
IDRCell	56.33	45.29
MCA-SSL (ViT Small) ours	60.16	44.70

Table D10: HPA Dataset Benchmark Scores

Model	**Task 1**	**Task 2**	**Task 3**
DINO (ViT Small) ours	91.31	68.55	43.13
OpenPhenom (ViT Small)	78.84	50.91	35.40
DINOv2 (ViT Small)	70.07	53.00	26.33
IDRCell (ViT Small)	70.86	49.90	30.90

Table D11: CP Dataset Benchmark Scores

Model	**Task 1**	**Task 2**	**Task 3**	**Task 4**
DINO (ViT Small) ours	88.90	51.73	21.83	12.57
OpenPhenom (ViT Small)	88.09	44.23	23.73	18.26
DINOv2 (ViT Small)	88.21	49.75	21.97	11.88
IDRCell (ViT Small)	79.29	51.43	20.63	07.25

D.1.1 Tested Configurations for SubCell

Here, we showcase the number of SubCell configurations that were tested for the CHAMMI benchmark. Each row presents results with different models. The input channel configurations of four models are bg, rgb, ybg, and rybg, where each letter defines the input channel. The general protein of interest (g) that localizes into different cellular compartments is a mandatory input to all models together with nucleus (b) reference channel. The other two reference channels, microtubules (r) and endoplasmic reticulum (y), are present in two model configurations. The HPA benchmark uses the original channel configuration of the SubCell paper. For the WTC benchmark, the 'bg' model is run twice with different input channels ('g' as membrane or protein) followed by concatenation of these extracted features. A similar approach is utilized for the CP benchmark, where three different inputs (Syto, WGA, and Mitotracker) are used for 'g' input channel. We have reported all the configurations we tested for all the different models types for WTC, HPA, and CP in D12, D13, and D14 respectively.

Table D12: SubCell WTC Scores

Model	**WTC**	**Task 1**	**Task 2**
MAE-CellS-ProtS-Pool bg	55.06	78.22	55.06
ViT-ProtS-Pool bg	33.70	57.51	33.70

Table D13: SubCell HPA Scores

Model	**HPA**	**Task 1**	**Task 2**	**Task 3**
MAE-CellS-ProtS-Pool rybg	64.58	96.26	84.01	45.15
MAE-CellS-ProtS-Pool rbg	71.63	95.59	88.07	55.19
MAE-CellS-ProtS-Pool ybg	66.93	95.03	79.73	54.12
MAE-CellS-ProtS-Pool bg	65.63	93.40	79.85	51.41
ViT-ProtS-Pool rybg	76.83	99.05	91.00	62.67
ViT-ProtS-Pool rbg	76.52	97.89	88.93	64.11
ViT-ProtS-Pool ybg	74.48	97.73	83.03	65.92
ViT-ProtS-Pool bg	72.96	96.06	82.70	63.23

Table D14: SubCell CP Scores

Model	CP	Task 1	Task 2	Task 3	Task 4
MAE-CellS-ProtS-Pool ybg	28.38	69.42	51.51	22.92	10.70
ViT-ProtS-Pool ybg	28.25	87.47	54.91	19.23	10.59

D.2 HPAv23 at 256x256

HPAv23 at 256x256 is a version of the original SubCell training images where the resolution of the images has been reduced from 1024x1024 to 256x256 with a resize. This transformation was done to reduce the compute time, and storage taken by the test set. We ran protein localization with HPAv23 at 256x256 in both of its configurations: challenge_cats in D15 and all_unique_cats in D16.

Table D15: Protein Localization (Challenge Classification Labels)

Model	Macro AP	Micro AP
DINO (ViT Small) ours	58.87	80.47
OpenPhenom (ViT Small)	49.13	75.75
DINOv2 (ViT Small)	53.76	77.01
SubCell (ViT Base)	69.33	84.79
IDRCell (ViT Small)	44.05	72.86

Table D16: Protein Localization (Unique Classification Labels)

Model	Macro AP	Micro AP
DINO (ViT Small) ours	44.38	78.07
OpenPhenom (ViT Small)	35.98	73.13
DINOv2 (ViT Small)	39.67	74.84
SubCell (ViT Base)	52.60	82.58
IDRCell (ViT Small)	44.05	72.86

D.3 JUMP-CP1 Compounds

Original JUMP-CP1 images were published with normalized (median absolute deviation *MAD-robustize*) well-level (replicate) CellProfiler features. Those features also include the ones that were extracted from brightfield images, for fair comparison those features were excluded. We also processed raw features by ofurselves: the same features were selected as in the paper version (except for features from brightfield channels) and performed ZCA-whitening (*spherize*) with pyCytominer in a similar way as we did for deep learning features. We also report the results obtained with Cell Painting CNN (Moshkov et al., 2024), feature post-processing was the same as for other deep learning features. Alongside the metrics *JUMP-CP1* and *JUMP-CP2*, we also report the *Active fraction*, that is a fraction of phenotypically active compounds versus negative controls and *mAP*-s from those active compounds contribute to *JUMP-CP1* result (Kalinin et al., 2025), otherwise *mAP* for non-active compounds would be zero. We reported our numbers with active fraction in D17.

Table D17: Phenotypic quality

Model	Active fraction	JUMP-CP1	JUMP-CP2
CellProfiler (paper)	81.70%	58.71	04.00
CellProfiler (ours)	99.02%	74.12	03.61
Cell Painting CNN	98.04%	77.45	06.80
DINO (ViT Small) ours	94.44%	76.32	06.79
OpenPhenom (ViT Small)	96.08%	74.26	04.99
DINOv2 (ViT Small)	94.44%	75.84	07.03
SubCell (ViT Base)	95.42%	77.60	07.44
IDRCell (ViT Small)	93.46%	72.37	04.98

D.4 IDR-17

IDR-17 is benchmarking based on a chemical–genetic interaction map of small molecules using high-throughput imaging in cancer cells. Add all the eight different cell lines, and the composite scores

We are going to be reporting all three metrics we have: ROC AUC scores in D20, Recall@50 in D19, Recall@100 in Table D18.

Table D18: Recall@100 Scores with Different Models

Cell Line	DINOv2	SubCell	OpenPhenom	BoC	IDRCell
HCT116 02-006	54.81	52.88	52.88	51.92	49.04
HCT116 02-008	62.79	60.47	60.47	62.79	62.79
HCT116 02-030	27.12	27.12	30.51	27.12	27.12
HCT116 02-031	54.29	57.14	54.29	54.29	51.43
HCT116 104-001	23.81	28.57	25.40	23.81	26.98
HCT116 104-004	41.10	39.73	36.99	39.73	36.99
HCT116 104-007	32.91	35.44	32.91	34.18	32.91
HCT116 104-008	39.58	40.63	39.58	39.58	34.38
Average	**42.05**	**42.75**	**41.63**	**41.68**	**40.20**

Table D19: Recall@50 Scores for Different Models

Cell Line	DINOv2	SubCell	OpenPhenom	BoC	IDRCell
HCT116 02-006	28.85	28.85	27.88	30.77	28.85
HCT116 02-008	46.51	46.51	46.51	44.19	44.19
HCT116 02-030	15.25	15.25	16.95	15.25	15.25
HCT116 02-031	31.43	28.57	28.57	31.43	31.43
HCT116 104-001	17.46	15.87	17.46	19.05	15.87
HCT116 104-004	23.29	20.55	21.92	23.29	20.55
HCT116 104-007	18.99	20.25	18.99	21.52	21.52
HCT116 104-008	19.79	19.79	19.79	18.75	17.71
Average	**25.20**	**24.46**	**24.76**	**25.53**	**24.42**

Table D20: AUC ROC Scores for Different Models

Sample	DINOv2	SubCell	OpenPhenom	BoC	IDRCell
HCT116 02-006	82.40	82.97	81.72	83.35	81.08
HCT116 02-008	81.08	81.14	80.45	81.86	83.08
HCT116 02-030	67.43	67.37	66.71	65.76	65.74
HCT116 02-031	87.83	87.29	84.67	86.47	82.45
HCT116 104-001	64.97	65.00	63.63	63.89	61.97
HCT116 104-004	76.06	77.31	76.88	76.01	76.90
HCT116 104-007	64.91	71.04	72.66	63.77	72.40
HCT116 104-008	75.55	77.46	76.16	76.00	75.01
Average	**75.03**	**76.20**	**75.36**	**74.64**	**74.83**

D.5 CellPHIE

Here, we report all the statistics for the CellPHIE benchmark in Table D21

Table D21: Comparison of Neuron-Features with Different Models

Neuron-Features	AUC	F1	Precision	Recall
CellProfiler	78.32	77.44	74.44	81.14
DINOv1 (Pretrained on NF)	73.72	72.30	74.76	70.44
DINO (ViT Small) ours	80.51	77.45	79.91	75.54
OpenPhenom (ViT Small)	77.56	75.68	77.84	74.04
DINOv2 (ViT Small)	73.95	72.27	76.29	68.97
SubCell (ViT Base)	71.24	70.60	74.26	67.78

D.6 RBC-MC

Table D22: Comparision of RBC-MC with Different Models

Model	Accuracy on Swiss	Accuracy on Canadian	Overall Accuracy
DINO-BoC	68.34%	65.06%	66.70%
IDRCell	55.85%	51.18%	53.50%
DINOv2	59.41%	55.35%	57.40%
OpenPhenom	64.43%	61.05%	62.70%
SubCell	59.10%	53.5%	56.30%
MCA-SSL	62.35%	59.01%	60.70%
MCA-SupC	55.40%	51.20%	53.30%
ChA-MAEViT	61.5%	56.60%	59.00%

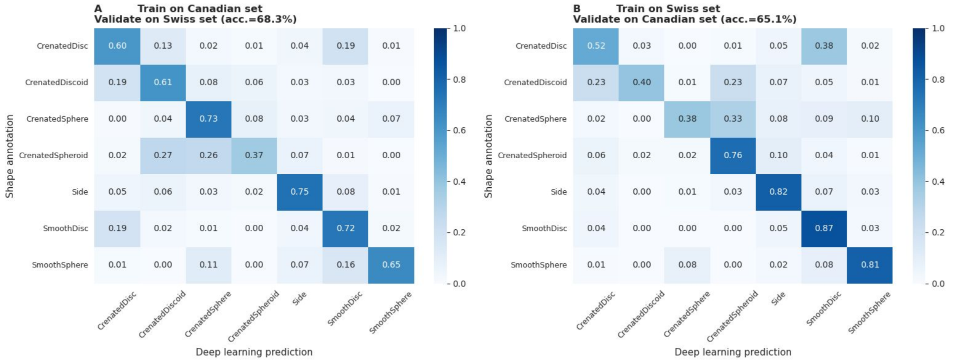

Figure D16: Confusion Matrices for RBC-MC Classification

E Disentanglement Experiments

To quantitatively assess the quality of the learned representations in separating biological signal from technical noise, we adopt the batch correction benchmarking framework from Arevalo et al. (2024). This framework is designed to evaluate how well a feature set disentangles batch signal (confounding variable) from biological signal (compound identity) by measuring metrics before and after the application of state-of-the-art batch correction algorithms. A high-quality feature set should: (1) require minimal correction in its raw state, and (2) maximize biological signal post-correction.

E.1 Experimental protocol

We evaluate performance using Scenario 2 from Arevalo et al. (2024): the classification of 302 landmark compounds generated by three different laboratories using the same microscope type. In this scenario, the batch variable is the Laboratory ID and the biological variable is the Compound. We assess the profiles using the population-averaged well-level approach to compute profiles. We compare three feature models: (1) CellProfiler Baseline: The original raw morphological features extracted using the conventional image analysis pipeline. (2) IDRCell Features: Features extracted using a ViT-Small DINO-BoC model trained on the smaller, heterogeneous IDRCell100K dataset ($\sim$ 100K images). (3) `CHAMMI-75` Features: Features extracted using our proposed ViT-Small DINO-BoC model trained on the full `CHAMMI-75` Large dataset. Based on the original study's findings, we focus on Seurat CCA as the optimal batch correction method for this scenario, which we apply to correct the features from all three models. Following standard practice, we report the aggregate score of four batch correction metrics, and six biological metrics, and the detail of these metrics is also reported for all three evaluated methods.

E.2 Results

The main results reported in Figure E17 highlight the following trend: (1) baseline state (no correction): `CHAMMI-75` features exhibit the best performance at the baseline level, yielding a higher raw biological signal, demonstrating better initial disentanglement of batch effects compared to both baselines. This indicates that pre-training on the highly diverse and curated `CHAMMI-75` dataset yields representations that are inherently more robust to cross-site technical variation. (2) Post-correction state: after applying the Seurat CCA batch correction method, `CHAMMI-75` features continue to facilitate the best performance, resulting in the highest biological signal among all feature sets. The performance of `CHAMMI-75` features is 1.7% better than CellProfiler features, and 11.8% better than IDRCell features, all after correction. Detailed results of batch correction metrics are reported in Figure E18 for the `CHAMMI-75` features, in Figure E19 for IDRCell features, and in Arevalo et al. (2024) for CellProfiler features.

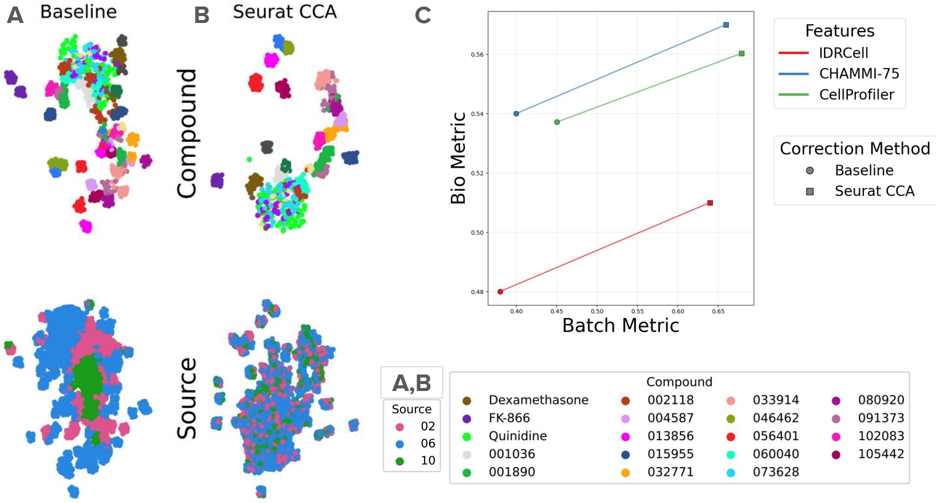

Figure E17: Disentanglement of feature representations using batch-correction on the JUMP-CP dataset, following Scenario 2 from the framework by Arevalo et al. (2024). A) UMAP visualization of raw DINO-BoC features learned from `CHAMMI-75` and aggregated at the well-level. B) UMAP visualization of corrected DINO-BoC features from A corrected with the Seurat CCA algorithm. C) Scatter plot of batch and biological scores (x and y axes, respectively) for three feature representations: IDRCell in red (ViT-small trained with IDRCell dataset), `CHAMMI-75` in blue (ViT-small trained with `CHAMMI-75`), and CellProfiler in green (classical features). In both axis, higher performance is better.

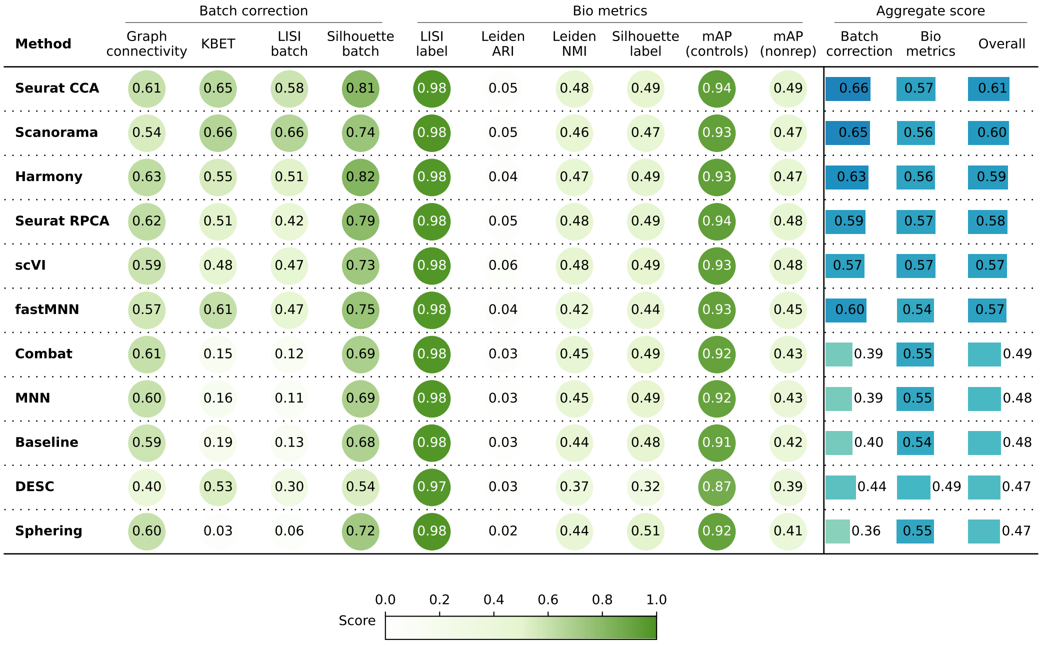

	Batch correction				Bio metrics						Aggregate score		
Method	Graph connectivity	KBET	LISI batch	Silhouette batch	LISI label	Leiden ARI	Leiden NMI	Silhouette label	mAP (controls)	mAP (nonrep)	Batch correction	Bio metrics	Overall
Seurat CCA	0.61	0.65	0.58	0.81	0.98	0.05	0.48	0.49	0.94	0.49	0.66	0.57	0.61
Scanorama	0.54	0.66	0.66	0.74	0.98	0.05	0.46	0.47	0.93	0.47	0.65	0.56	0.60
Harmony	0.63	0.55	0.51	0.82	0.98	0.04	0.47	0.49	0.93	0.47	0.63	0.56	0.59
Seurat RPCA	0.62	0.51	0.42	0.79	0.98	0.05	0.48	0.49	0.94	0.48	0.59	0.57	0.58
scVI	0.59	0.48	0.47	0.73	0.98	0.06	0.48	0.49	0.93	0.48	0.57	0.57	0.57
fastMNN	0.57	0.61	0.47	0.75	0.98	0.04	0.42	0.44	0.93	0.45	0.60	0.54	0.57
Combat	0.61	0.15	0.12	0.69	0.98	0.03	0.45	0.49	0.92	0.43	0.39	0.55	0.49
MNN	0.60	0.16	0.11	0.69	0.98	0.03	0.45	0.49	0.92	0.43	0.39	0.55	0.48
Baseline	0.59	0.19	0.13	0.68	0.98	0.03	0.44	0.48	0.91	0.42	0.40	0.54	0.48
DESC	0.40	0.53	0.30	0.54	0.97	0.03	0.37	0.32	0.87	0.39	0.44	0.49	0.47
Sphering	0.60	0.03	0.06	0.72	0.98	0.02	0.44	0.51	0.92	0.41	0.36	0.55	0.47

Figure E18: Detailed report of batch correction metrics for the DINO-BoC model trained with `CHAMMI-75`

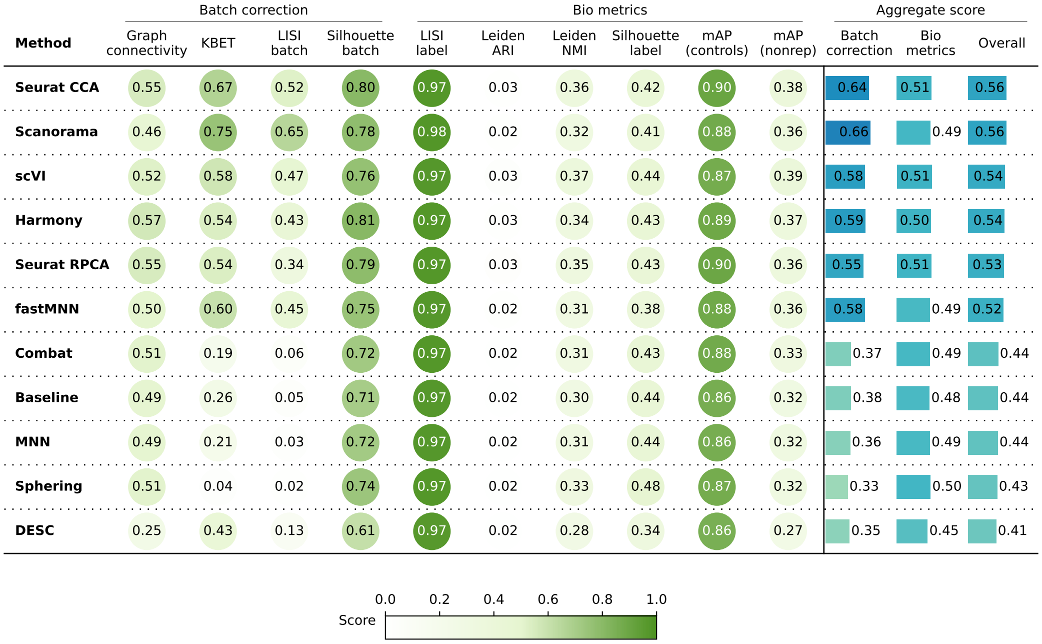

	Batch correction				Bio metrics						Aggregate score		
Method	Graph connectivity	KBET	LISI batch	Silhouette batch	LISI label	Leiden ARI	Leiden NMI	Silhouette label	mAP (controls)	mAP (nonrep)	Batch correction	Bio metrics	Overall
Seurat CCA	0.55	0.67	0.52	0.80	0.97	0.03	0.36	0.42	0.90	0.38	0.64	0.51	0.56
Scanorama	0.46	0.75	0.65	0.78	0.98	0.02	0.32	0.41	0.88	0.36	0.66	0.49	0.56
scVI	0.52	0.58	0.47	0.76	0.97	0.03	0.37	0.44	0.87	0.39	0.58	0.51	0.54
Harmony	0.57	0.54	0.43	0.81	0.97	0.03	0.34	0.43	0.89	0.37	0.59	0.50	0.54
Seurat RPCA	0.55	0.54	0.34	0.79	0.97	0.03	0.35	0.43	0.90	0.36	0.55	0.51	0.53
fastMNN	0.50	0.60	0.45	0.75	0.97	0.02	0.31	0.38	0.88	0.36	0.58	0.49	0.52
Combat	0.51	0.19	0.06	0.72	0.97	0.02	0.31	0.43	0.88	0.33	0.37	0.49	0.44
Baseline	0.49	0.26	0.05	0.71	0.97	0.02	0.30	0.44	0.86	0.32	0.38	0.48	0.44
MNN	0.49	0.21	0.03	0.72	0.97	0.02	0.31	0.44	0.86	0.32	0.36	0.49	0.44
Sphering	0.51	0.04	0.02	0.74	0.97	0.02	0.33	0.48	0.87	0.32	0.33	0.50	0.43
DESC	0.25	0.43	0.13	0.61	0.97	0.02	0.28	0.34	0.86	0.27	0.35	0.45	0.41

Figure E19: Detailed report of batch correction metrics for the DINO-BoC model trained with IDRCell

This confirms that the learned CHAMMI-75 feature space is structured in a way that is amenable to correction, allowing the batch correction algorithm to remove confounding noise without destroying the underlying biological coherence. Importantly, features learned with the IDRCell dataset consistently perform worse than the CellProfiler baseline in both the raw and corrected states. This contrast highlights that simply aggregating diverse data is insufficient; the scale, comprehensive heterogeneity, and careful curation embedded in CHAMMI-75 are necessary factors for learning disentangled, biologically meaningful representations.

F Qualitative analysis of feature space

To visualize the global structure of the feature space learned by models trained on CHAMMI-75 , we performed a qualitative analysis using UMAP projection on single-channel features extracted from a balanced, single-cell sample of all 75 source studies.

F.1 Experimental protocol

We sampled approximately 1,000 single-cell, multi-channel crops from imges in each of the 75 source studies, resulting in 196,660 individual single-channel images. We then used three representative pre-trained ViT models to compute fixed-length feature representations for each individual single-channel image: (1) CHAMMI-75 DINO-BoC: our proposed model trained with CHAMMI-75 . (2) DINOv2: the generalist vision model adapted for microscopy features. (3) OpenPhenom: the channel-adaptive model trained on fixed-channel Cell Painting data. Given the difference in number of channels, we do not display multi-channel images in the visualizations because the bag-of-channels approach yields a variable-length feature representation across studies. We collect single-channel features with all models, including the channel-adaptive OpenPhenom model.

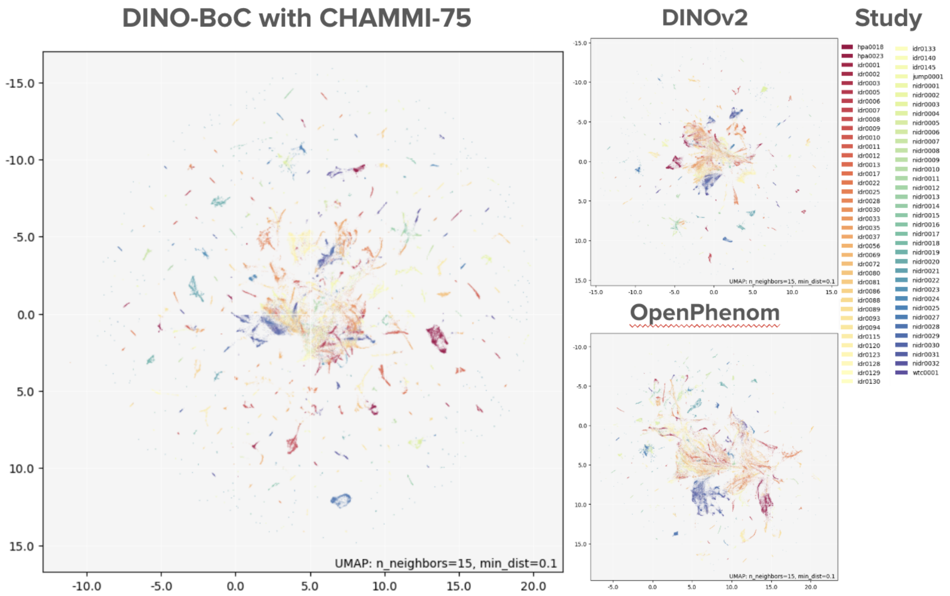

Figure F20: UMAP visualizations of the feature spaces obtained with three ViT-small models: DINO-BoC trained with `CHAMMI-75` , DINOv2, and OpenPhenom. The colors indicate source study, which is the dominant factor of variation in all three cases.

F.2 Results and Discussion

The UMAP visualizations for all three models (Figure DX) show that the feature space is primarily segregated by the source study ID (technical domain), rather than being uniformly mixed. This result leads to two key interpretations: (1) domain sensitivity vs. invariance: self-supervised models, even when trained on highly diverse data, do not produce strictly domain-invariant representations in the raw feature space. Instead, they are domain-sensitive, clustering the input based on technical factors (e.g., image acquisition parameters, microscopy type, local processing) unique to each of the 75 source studies. This strong inter-study differentiation highlights the genuine heterogeneity of `CHAMMI-75` . (2) Consistency with quantitative results: this qualitative observation aligns with our findings in the Disentanglement Experiments (Appendix D.1): since the technical signature remains present, a post-processing step like batch correction is necessary to remove this study-specific bias and maximize the detection of subtle biological signals. The strong clustering visible in the UMAP indicates that the high performance of `CHAMMI-75` features (Section 5.1) is achieved not by erasing the domain difference entirely, but by encoding these differences in a way that is highly distinguishable and amenable to correction. Further qualitative exploration by coloring the UMAP plots with other metadata fields (such as channel configuration or biological condition) reveals strong intra-study consistency, but the inter-study structure remains dominated by the technical source.

G Experiments

G.1 Model Configurations and parameters

All the models we trained have similar model configurations to have a fair comparison.

G.1.1 Multi-channel strategies

Multi-Channel Attention (MCA). Multi-channel attention models allow a ViT network to compute attention across channels. These networks work by unraveling the channel dimension into the sequence input of the vision transformer and use learned channel embeddings in order to denote which tokens belong to which channels (similar to positional encodings). These embeddings are learned per channel type (e.g. DNA and RNA encodings) and effect all tokens in a given channel the same way. MCA was modified to use masked attention to handle mixed sequence lengths. Channels were padded with 0 tokens if sequences were of smaller length and an attention bias was used for the softmax to ignore these tokens. Models were trained with a patch size or 16, for 100 epochs in total.

Bag of Channels (BoC). Bag of Channels models is a strategy where we break all multi-channel images into single and the model learns from one single channel at a time. A drawback of this strategy is that the model does not learn inter-channel correlations as it only learns from one channel at a time. During evaluation, we usually concatenate the feature embedding space of all different test evaluation channels.

G.1.2 Types of SSL Models

DINO. DINO is a self-supervised framework that employs a student-teacher network to learn representations in imaging (Caron et al., 2021).

MAE. MAE is a self-supervised framework that masks random patches and reconstructs the missing pixels (He et al., 2022).

SimCLR. SimCLR is a self-supervised framework that uses data augmentations to perform contrastive learning with images. (Chen et al., 2020).

G.1.3 Model Parameters

DINO BoC. The default training parameters of the DINO model were used except - the learning rate changed to 5e-5. Batch sizes varied according to model sizes with 256, 128, and 32 used for ViT Small, ViT Base, and ViT Large respectively. We ran the model with horizontal and vertical flips for augmentations.

MAE BoC. The default training parameters of the MAE model were used except - learning rate changed to 5e-4, weight decay changed to 0.04, warm-up epochs changed to 10, and the number of epochs changed to 100 epochs. Batch sizes varied according to model sizes with 1024, 768, and 384 used for ViT Small, ViT Base, and ViT Large respectively. We ran the model with horizontal and vertical flips for augmentations.

SimCLR BoC. The default training parameters of the SimCLR model were used except - learning rate changed to 5e-5, weight decay changed to 0.04, warm-up epochs changed to 10, and the number of epochs changed to 100 epochs. The model was run with random resized crop with scale (0.2, 1.0), RandomHorizontalFlip, RandomVerticalFlip, and Gaussian blurring to develop two samples.

Channel-ViT DINO. Channel-ViT DINO replaces the fixed channel ViT backbone with a MCA ViT backbone and uses the standard DINO SSL algorithm to optimize the network. The multi channel id metadata was used to gather multi-channel images. DINO augmentations were than ran with horizontal and vertical flips with 8 local crops and 2 global crops. DINO global crops were 224x224 and local crops were 96x96 with crop ratios of 0.4-1.0 and 0.05-0.4 respectively. Learning rate was warmed up from 1e-6 to to 0.0001 for all models over 10 epochs. Teacher temperature was warmed up from 0.04 to 0.07 over 30 epochs. Weight Decay was warmed up from 0.04 to 0.04 over 10 epochs. The AdamW optimizer was used with default parameters other than those discussed previously. We trained with standard cosine annealing schedules as defined in (Caron et al., 2021). MCA DINO was modified to use masked attention to handle mixed sequence lengths. Channels were padded with 0 tokens if sequences were of smaller length and an attention bias was used for the softmax to ignore these tokens. Models were trained with a patch size or 16, for 100 epochs in total.

Channel-ViT SimCLR. Channel-ViT SimCLR replaces the fixed channel ViT backbone with an MCA ViT backbone and uses the standard SimCLR SSL algorithm. The multi_channel_id metadata was used to gather multi-channel images. The model was run with random resized crop with scale (0.2, 1.0), RandomHorizontalFlip, RandomVerticalFlip, and Gaussian blurring to develop two samples. The learning rate used was 5e-5.

Channel-ViT MAE. Channel-ViT MAE replaces the fixed channel ViT backbone with an MCA ViT backbone and uses the standard MAE SSL algorithm. The multi_channel_id metadata was used to gather multi-channel images. The model was run with RandomHorizontalFlip, and RandomVerticalFlip. The learning rate used was 5e-5.

G.1.4 Supervised Baseline

ViT-small models were trained with a fixed number of channels per dataset in CHAMMI. A drop path rate of 0.2 was used for each block in the transformer. The AdamW optimizer was used with a learning rate of 0.001 and weight decay of 0.4. Augmentations of randomly resized crops, horizontal flips, rotations, gaussian blurring and self-normalization were used. A prediction head was used to go from the CLS token to the number of classes in each dataset. This was a linear head with L1 and L2 norms applied, with lambdas of 0.01. A cosign annealing along the learning rate was applied. No warmup was used. Standard cross entropy loss was used to train the network with 8 L40S GPUs for 60-100 epochs, depending on when scores stopped improving. The maximum score along the epochs was then used for the result of each CHAMMI dataset in the score G23.

Table G23: Summary of IID Mean, CHAMMI Score for Supervised Baseline)

Model	IID Mean	CHAMMI Score	WTC	HPA	CP
Supervised Baseline	78.76	54.56	65.21	71.84	26.64

G.2 Resources Used

7-10 GPUs of NVidia A6000, L40S, and L40 were used with servers having 96 CPUs and server memory of 512 GB.

G.3 Scaling Computations

Here, we describe how the computation varies for Bag of Channels and Multi-Channel Attention models. Figure G21 showcases how much more compute time Multi-channel models take as compared to Bag of Channels models.

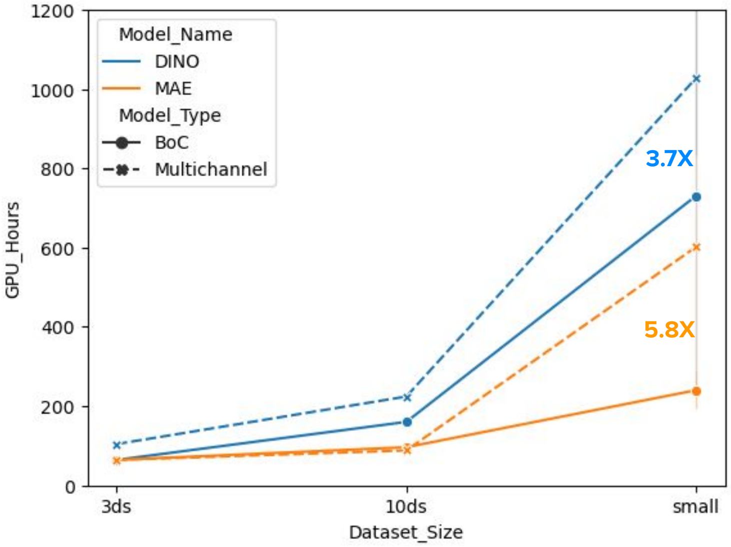

Figure G21: Compute time in GPU hours (vertical axis) of model training when the dataset size is increased (horizontal axis). The dataset sizes are 3ds (100K images), 10ds (150K images), and small (74ds with 560K images).

G.4 Additional Experiments

G.4.1 Dataset Scaling with HPAv23 at 256x256

In our paper, we have mainly used CHAMMI as an indicator of model performance boosting as we increase number of sampled images used for training. Table G24 showcases similar scaling HPAv23 at 256x256 is used.

Table G24: DINO Dataset Scaling Using HPAv23 at 256x256.

Dataset Configuration	Macro AP
3 Datasets	41.00
10 Datasets	53.40
`CHAMMI-75` Small	54.92
`CHAMMI-75` Large	59.17

G.5 Fine-Tuning Models on Downstream Tasks

While our experiments successfully utilize the pre-trained `CHAMMI-75` model with only a linear probe (frozen backbone) to achieve state-of-the-art results, researchers may explore fine-tuning for specific, complex downstream tasks. However, based on our experience, we caution that full fine-tuning of multi-channel models for cell phenotyping is often challenging due to the scarcity of large, high-quality supervised labels, leading frequently to poor generalization and rapid overfitting.

When to avoid fine-tuning (default recommendation). We strongly recommend avoiding fine-tuning when the downstream task relies on subtle phenotypic differences without clean, manually validated labels (e.g., weak treatment labels in small screens). Also when the available labeled data is small, as a ViT model (even small size) tends to quickly overfit to the batch-specific signal in the training set. In such cases, extracting features with a frozen `CHAMMI-75` backbone and training a simple linear classifier (as done in our HPAv23 and RBC-MC benchmarks) is the most robust and computationally efficient approach.

Best practices for fine-tuning (only if necessary). If a researcher must fine-tune the backbone (e.g., if highly clean, validated annotation sets like those in HPAv23 are available), they should follow these steps: (1) Input Standardization: the input images must follow the same preprocessing steps applied during `CHAMMI-75` training, which include intensity normalization by applying 0.1% and 99.9% percentile clipping per channel, followed by per-channel self-normalization. (2) Spatial cropping: use single-cell coordinates to ensure crops are centered on relevant cellular content. Architecture adaptation (bag-of-channels): for a target task with N channels, adapt the BoC architecture by fixing N. This involves replicating the pre-trained weights of the first layer (the convolution or patch embedding layer) N times to accept the N-channel input image. The remainder of the model architecture (the transformer blocks) remains unchanged and loaded with the pre-trained weights. (3) Training protocol: employ conservative training schedules with a very low learning rate (e.g., 10^{-5} to 10^{-6}) for the feature extractor backbone. Use strong regularization (e.g., high weight decay) to prevent catastrophic forgetting of the general knowledge learned from `CHAMMI-75` .

We reiterate that none of the results reported in this paper were obtained through fine-tuning; instead, we found that linear probing yielded the most stable and generalizable performance across all phenotyping tasks.